

POLYTECHNIC SCHOOL OF THE UNIVERSITY OF SAO PAULO
DEPARTMENT OF MECHATRONIC ENGINEERING AND MECHANICAL SYSTEMS

NILTON BARBOSA DA ROSA JUNIOR

**TEST BENCH FOR DEVELOPMENT OF IMAGING RECONSTRUCTION
ALGORITHMS FOR ULTRASOUND TOMOGRAPHY**

Sao Paulo
2020

NILTON BARBOSA DA ROSA JUNIOR

**TEST BENCH FOR DEVELOPMENT OF IMAGING RECONSTRUCTION
ALGORITHMS FOR ULTRASOUND TOMOGRAPHY**

Revised Version

Dissertation presented to the Polytechnic
School of the University of Sao Paulo to
obtain a Master's Degree in science.

Concentration area: Mechanical Engineering
on Control and Automation.

Advisor: Dr. Chi Nan Pai.

Sao Paulo
2020

Autorizo a reprodução e divulgação total ou parcial deste trabalho, por qualquer meio convencional ou eletrônico, para fins de estudo e pesquisa, desde que citada a fonte.

Este exemplar foi revisado e corrigido em relação à versão original, sob responsabilidade única do autor e com a anuência de seu orientador.

São Paulo, 21 de Outubro de 2020

Assinatura do autor: Nilton Barbosa da Rosa Junior

Assinatura do orientador: Pai Chi Nan

Catálogo-na-publicação

Barbosa da Rosa Junior, Nilton
TEST BENCH FOR DEVELOPMENT OF IMAGING
RECONSTRUCTION ALGORITHMS FOR ULTRASOUND TOMOGRAPHY /
N. Barbosa da Rosa Junior -- versão corr. -- São Paulo, 2020.
62 p.

Dissertação (Mestrado) - Escola Politécnica da Universidade de São Paulo. Departamento de Engenharia Mecânica.

1.IMAGEAMENTO (BIOENGENHARIA) (RECONSTRUÇÃO)
2.TOMOGRAFIA 3.ULTRASSONOGRÁFIA 4.RESPIRADORES MECÂNICOS
5.PULMÃO (MONITORAMENTO) I.Universidade de São Paulo. Escola Politécnica. Departamento de Engenharia Mecânica II.t.

NAME: ROSA JUNIOR, Nilton Barbosa.

TITLE: Test Bench for Development of Imaging Reconstruction Algorithms for Ultrasound Tomography.

Dissertation presented to the Graduate Program in Mechanical Engineering at the Polytechnic School, University of Sao Paulo, Brazil.

Approval Date:

Evaluation Committee

Dr. _____

Institution _____

Judgment _____

Dr. _____

Institution _____

Judgment _____

Dr. _____

Institution _____

Judgment _____

ACKNOWLEDGEMENTS

I thank God for protecting and giving me strength throughout the years that I have done this research. I also want to thank all my family members that have supported me, making it possible to accomplish my master's degree.

I thank Professor Chi-Nan Pai, my advisor, for assisting me and providing a critical thinking about how to do research, but not only this, but also for showing me the paths and opportunities that being a researcher provides.

I thank Timoteo Francisco de Oliveira and Rafael Mikio Nakanishi for helping during the manufacturing process of ultrasound transducers. Also, I thank all friends from the Ultrasound Laboratory.

I thank Professor Sergio Shiguemi Furuie from the Biomedical Engineering Laboratory and his master's degree students for all the help.

I thank the Conselho Nacional de Desenvolvimento Científico e Tecnológico (CNPq) for the grant.

RESUMO

ROSA JUNIOR, N. B. Bancada de testes para desenvolvimento de algoritmos de reconstrução de imagens para a tomografia por ultrassom. Dissertação (Mestrado) – Programa de Pós Graduação em Engenharia Mecânica, Escola Politécnica da Universidade de São Paulo, São Paulo, 2020.

Exames de imagem são importantes para monitorar pacientes sob ventilação mecânica na Unidade de Terapia Intensiva (UTI). Um exame comum para imagens anatômicas é a tomografia computadorizada por raio-x. No entanto, esse método de imagem tem suas desvantagens, tais como a necessidade de remover o paciente da UTI, aumentando o risco de complicações; o uso de radiação ionizante, a qual é prejudicial ao ser usada continuamente. Para imagens funcionais, a Tomografia por Impedância Elétrica (EIT) é uma técnica recente de imageamento para monitorar continuamente as funções pulmonares a beira do leito nas UTIs. No entanto, a EIT ainda apresenta baixa resolução espacial e baixa precisão de localização. A tomografia por ultrassom (TUS) tem o potencial de proporcionar uma melhor imagem funcional pulmonar. Contudo, essa técnica nunca foi usada antes. O objetivo deste trabalho é desenvolver uma bancada de testes experimental, simular um sistema TUS e avaliar sua viabilidade para imagens funcionais pulmonares. 9 transdutores mono-elemento foram fabricados com cerâmica piezoelétrica de 500 kHz, e foram caracterizados através da medição de sua impedância elétrica, resposta do pulso-eco, pressão acústica transmitida e sensibilidade, através das técnicas de transmissão e de reflexão. 8 transdutores fabricados foram selecionados para serem montados em um cilindro de madeira que foi colocado dentro de um tanque cheio de água. Um transdutor foi usado como emissor e quatro outros como receptores, com um phantom colocado em várias posições no interior. Os resultados da impedância elétrica e de pulso-eco mostraram frequências abaixo de 200 kHz com amplitudes entre 20 e 300 mV (pico a pico). Além disso, as medidas de pressão acústica e de sensibilidade mostraram que os transdutores fabricados têm frequências centrais em torno de 170 kHz com pressão acústica transmitida entre 8,9 kPa e 148 kPa e respostas de sensibilidade de 15,24 V/MPa a 59 V/MPa. A avaliação da bancada de testes também mostrou sinais compatíveis com o esperado, mostrando que essa bancada de TUS pode ser usada para o desenvolvimento de algoritmos para reconstrução de imagens.

Palavras-chave: Tomografia por ultrassom. Transdutor PZT. Monitoramento pulmonar. Ventilação mecânica.

ABSTRACT

ROSA JUNIOR, N. B. Test bench for development of reconstruction imaging algorithms of ultrasound tomography. Dissertação (Mestrado) – Programa de Pós Graduação em Engenharia Mecânica, Escola Politécnica da Universidade de São Paulo, São Paulo, 2020.

Imaging exams are important to monitor patients under mechanical ventilation in the Intensive Care Unit (ICU). A common exam for anatomical imaging is the Computed Tomography. However, this imaging method has its drawbacks, such as the need to remove the patient from the ICU, which increases the risk for complications; use of ionizing radiation, which is harmful if used continuously. For functional imaging, Electrical Impedance Tomography (EIT) is a recent imaging technique to continuously monitor pulmonary functions at the bedside in ICUs. Nevertheless, EIT still presents low spatial resolution and low location accuracy. The Ultrasound Tomography (UST) has the potential to provide better pulmonary functional imaging. However, it has never been used before. The aim of this work is to develop an experimental test bench, to simulate an UST system, and to evaluate its feasibility for pulmonary functional imaging. 9 single-element transducers were manufactured by using 500 kHz piezoelectric ceramic and were characterized by measuring its electrical impedance, pulse-echo response, transmitted acoustic pressure and sensitivity, through the transmission and reflection techniques. 8 of the manufactured transducers were selected to be assembled on a wooden cylinder that was placed inside a tank filled with water. One transducer was used as emitter and four others as receptors, with a phantom placed in several positions inside. The electrical impedance and the pulse-echo results showed frequencies below 200 kHz with amplitudes between 20 and 300 mV (peak-to-peak). Moreover, the acoustic pressure and sensitivity measurements showed that the manufactured transducers have central frequencies around 170 kHz with transmitted acoustic pressure between 8.9 kPa and 148 kPa, and sensitivity responses from 15.24 V/MPa to 59 V/MPa. The evaluation of the test bench also showed signals compatible to expected, showing the feasibility of this UST test bench for the development of reconstruction imaging algorithms.

Keywords: Ultrasound tomography. PZT transducer. Lung monitoring. Mechanical ventilation.

FIGURE LIST

Figure 1: Time of flight of 4 transmitted ultrasound waves.....	18
Figure 2: Time and frequency domain of sinusoidal pulses. (a) 1 pulse and (b) 10 pulses.	19
Figure 3: Overview of a prototype system for developing reconstruction imaging algorithms of UST.....	20
Figure 4: PZT transducer schematic. Units in millimeters.....	21
Figure 5: Schematic for the pulse-echo technique.....	24
Figure 6: Top view of the schematic for measuring f_R . Units in millimeters.....	25
Figure 7: Sensitivity response of the hydrophone: (a) from 30 kHz to 1 MHz (b) 1 MHz to 20 MHz.	25
Figure 8: Block diagram to calculate the acoustic pressure.	27
Figure 9: Top view of the acoustic tank for measuring the acoustic pressure using a sinusoidal pulse. Units in millimeters.....	28
Figure 10: Top view of the acoustic tank for measuring the acoustic pressure using a square pulse. Units in millimeters.....	29
Figure 11: Top view of the acoustic tank with a waveform generator and measuring with RTs. Units in millimeters.....	30
Figure 12: Top view of the acoustic tank with a Pulser and measuring with RTs.	31
Figure 13: Schematic of the test bench. Units in millimeters.....	31
Figure 14: Test bench placed in a tank filled with water. Units in millimeters.	32
Figure 15: Schematic of the complete system to transmit and receive signals for UST. Units in millimeters.	33
Figure 16: Manufactured single-element PZT ultrasound transducer. Units in millimeters....	34
Figure 17: Electrical impedance of PZT ceramic and manufactured transducers. (a) Transducer 2, (b) Transducer 5 and (c) Transducer 8.....	35
Figure 18: The maximum amplitude (V_{PP}) and resonance frequency of each transducer manufactured.	36
Figure 19: Measured acoustic pressure distribution using a hydrophone for capturing signal and a sinusoidal pulse for driving T1.....	39
Figure 20: Measured acoustic pressure profile at $Z = 10$ mm when driving transducers with a sinusoidal pulse.....	40
Figure 21: Ultrasound wave propagation, ET and Hydrophone.....	41

Figure 22: Measured acoustic pressure distribution using a hydrophone for capturing signals and a square pulse for driving the transducers.	42
Figure 23: Measured acoustic pressure profile at $Z = 10$ mm when driving transducers with a square pulse.	43
Figure 24: Time domain and FFT plots of acoustic pressure at $X = 0$ mm and $Z = 10$ mm. (a) Square Pulse Source and (b) Sinusoidal Pulse Source.....	43
Figure 25: Calculated acoustic pressure distributions for frequencies bellow 500 kHz using a hydrophone for capturing signals and a square pulse for driving the transducers.....	44
Figure 26: Measured voltage distributions using transducers as receivers and driving T1 with a sinusoidal pulse.	46
Figure 27: Measured voltage profiles at $Z = 10$ mm when receiving with transducers and driving T1 with a sinusoidal pulse.	47
Figure 28: Ultrasound wave propagation, ET and RT.	48
Figure 29: Measured voltage distributions using transducers as receivers and driving T1 with a square pulse.....	49
Figure 30: Measured voltage profiles at $Z = 10$ mm when receiving with transducers and driving T1 with a square pulse.	50
Figure 31: (a) Manufactured phantom and (b) the test bench after assembling.	52
Figure 32: Recorded signals with phantom at position A.	52
Figure 33: Recorded signals with phantom at position B.	53
Figure 34: Recorded signals with phantom at position C	54
Figure 35: Recorded signals with phantom at position D.	55
Figure 36: Recorded signals with no phantom placed inside the test bench.	55
Figure 37: Recorded signals for each transducer.	56

TABLE LIST

Table 1: Measured f_R for each transducer. Units in kHz.....	37
Table 2: Peak-to-peak amplitudes of captured signals for driving transducer with a sinusoidal pulse. Units in V_{PP}	37
Table 3: Attenuation coefficients for driving transducers with 150 kHz (red color) and 200 kHz (blue color) sinusoidal pulse. Units in dB.....	38
Table 4: Calculated sensitivity when driving transducers with a sinusoidal pulse.....	48
Table 5: Calculated when driving the transducers with a square pulse.	50

ABBREVIATION LIST

ARDS	Acute Respiratory Distress Syndrome
ALI	Acute Lung Injury
SARS	Severe Acute Respiratory Syndrome
ICU	Intensive Care Unit
MV	Mechanical Ventilation
PEEP	Positive End-Expiratory Pressure
CT	Computed Tomography
EIT	Electrical Impedance Tomography
UST	Ultrasound Tomography
CW	Continuous Wave
PZT	Lead Zirconate Titanate
CPVC	Chlorinated Polyvinyl Chloride
BNC	Bayonet Neill–Concelman
dB	Decibel
ET	Emitting Transducer
RT	Receiving Transducer
FFT	Fast Fourier Transform
IFFT	Inverse Fast Fourier Transform
HY	Calibrated needle hydrophone
S	Sensitivity
CS	Captured signal
AP	Measured acoustic pressure
PVC	Polyvinyl Chloride
T1	Transducer 1
T2	Transducer 2
T3	Transducer 3
T4	Transducer 4
T5	Transducer 5
T6	Transducer 6
T7	Transducer 7
T8	Transducer 8
T9	Transducer 9

SYMBOL LIST

Z_{MAT}	Acoustic impedance of the matching layer
Z_{PZT}	Acoustic impedances of the PZT ceramic
Z_{WATER}	Acoustic impedances of water
M_{TH}	Thickness of the matching layer
c_{MAT}	Speed of sound in the matching layer
f_{PZT}	PZT ceramic resonance frequency
V_{PP}	Peak-to-peak amplitude
f_i	frequency interval
f_R	Resonance frequency
f_C	Central resonance frequency
λ_{WATER}	Wavelength in water
c_{WATER}	Speed of sound in water
P_{WD}	Pulse width

SUMMARY

1	INTRODUCTION	14
2	BACKGROUND	17
3	MATERIALS AND METHODS	21
3.1	PZT ultrasound transducer	21
3.2	Characterization of PZT transducers	23
3.2.1	Electrical Impedance.....	23
3.2.2	Pulse-Echo technique.....	23
3.2.3	Resonance frequencies.....	24
3.2.4	Acoustic Pressure	25
3.2.5	Transmitting-Receiving Technique	29
3.3	Manufacturing and assembly of the test bench	31
3.4	Evaluation of the test bench	32
4	RESULTS AND DISCUSSIONS.....	34
4.1	PZT ultrasound transducer	34
4.2	Characterization Results.....	34
4.2.1	Electrical impedance.....	34
4.2.2	Pulse-echo technique	35
4.2.3	Resonance frequencies.....	36
4.2.4	Acoustic Pressures	39
4.2.5	Transmitting-Receiving technique.....	45
4.3	Manufactured test bench	51
4.4	Evaluation of the test bench	52
5	CONCLUSIONS	57
6	REFERENCES	59

1 INTRODUCTION

Acute respiratory syndromes have become one of the major causes of pulmonary diseases worldwide. A study published in 1967 was the first to address a respiratory-distress syndrome which did not respond to conventional methods of respiratory therapy. The patients developed an acute onset of tachypnea, which is a condition of rapid breathing, low levels of oxygen in the blood (hypoxemia), and loss of compliance after a variety of stimuli, leading to extra work during inspiration (ASHBAUGH et al., 1967).

During the American-European consensus conference in 1994, the term Acute Respiratory Distress Syndrome (ARDS) was defined as a syndrome characterized by the association of hypoxemia with inhomogeneous distribution of ventilation and perfusion without cardiac dysfunction. Acute Lung Injury (ALI) was also defined for a variety of gas exchange disorders, having ARDS as the most severe form of the disease. Moreover, different underlying diseases such as pulmonary (e.g. Aspiration, Pneumonia and Toxic inhalation) and non-pulmonary (e.g. Sepsis, Severe non-thoracic trauma and pancreatitis) may also be the cause of ARDS (LIPSON; BEEK, 2005) (RAGALLER; RICHTER, 2010).

Another sort of acute respiratory syndrome is the Severe Acute Respiratory Syndrome (SARS). This pulmonary disease was first reported in 2002, and it is caused by a highly contagious virus called coronavirus (CHENG et al., 2007). A novel coronavirus, known as SARS-CoV-2 or COVID-19, has emerged in 2019, and it rapidly spread throughout China and other countries, becoming a major global health concern (LAI et al., 2020). The main COVID-19 symptoms are fever, cough and fatigue, with the chance to develop pneumonia, ARDS, and secondary infections in severe cases (WANG et al., 2020).

Since there are few treatment methods available for severe cases of SARS and ARDS, the main therapy for patients admitted to Intensive Care Unit (ICU) is the Mechanical Ventilation (MV) (FAN et al., 2017) (YANG et al., 2020). Adjusting the MV parameters to lower end-inspiratory airway pressures, lower tidal volumes, and higher positive end-expiratory pressures (PEEPs) can improve survival in patients with ARDS (AMATO et al., 2015). Moreover, this strategy can also be used during the treatment of patients with SARS-CoV-2 (CASCELLA et al., 2020).

To improve the interaction MV-patient, and to avoid inappropriate use which could lead to lung and respiratory muscles injuries (barotrauma, volutrauma and myotrauma), graphical information from flow and pressure can be used to adjust the MV parameters

(BERTONI; SPADARO; GOLIGHER, 2020) (LIAN, 2010). Nevertheless, graphical waveforms reflect only overall lung function, failing to provide information on local functionality, which is important when adjusting the parameters of MV. Hence, imaging exams that can be used as alternatives for lung assessment to set the MV parameters are the Computed Tomography (CT) and Electrical Impedance Tomography (EIT) (CINEL; JEAN; DELLINGER, 2007).

CT imaging has helped to understand ARDS and how it affects the lungs, offering the recognition of normally aerated lung, and poorly/uninflated areas. In addition, the lung morphology determines the response to PEEP, recruitment maneuvers, and prone position in mechanically ventilated patients. However, despite having several advantages, CT is not used as a criterion for definition of ARDS because of the cost, the safety, the availability and the feasibility. Moreover, it also represents a life risk due to the need to move the patient to the radiology department (CHIUMELLO et al., 2013).

EIT has been an emerging imaging exam for pulmonary functional imaging to assess the lungs. This exam is non-invasive, available at the bed-side in ICUs and can provide real-time and continuous images of the lungs due to the absence of ionizing radiation (BALL et al., 2017). Through EIT imaging, the distributions of gas volume entering the lungs, regional characteristics of pulmonary structures, and discern about alveolar collapse and overdistention can be evaluated (TOMICIC; CORNEJO, 2019). Moreover, EIT also has the ability to identify dynamic changes in tidal recruitment, becoming an effective tool to determine an optimal PEEP (NIEMAN et al., 2017).

Although EIT has proven to be an important technique for lung assessments, its images still suffer from low spatial resolution for both ventilation and perfusion, and low positioning accuracy compared to other imaging exams (Steiner et al, 2008). Furthermore, EIT images only reflect changes in the impedance of lungs tissues, which means that existing conditions before monitoring cannot be evaluated (RIERA et al., 2011).

Our group is investigating the feasibility to use Ultrasound Tomography (UST) as a new and innovative imaging method for monitoring the lung function of mechanically ventilated patients. Using ultrasound waves, measurements of attenuation, speed of sound, reflection coefficients and time of flight are available for transmission and reflection reconstruction imaging algorithms, making it an imaging exam with high potential to provide more information about lung functions as well as real-time bedside monitoring.

UST has been widely researched for anatomical imaging of breasts. Some institutes and companies have developed prototype systems with single and multi-element transducers, different central frequencies and amount of transmitting and receiving transducers in order to make reconstruction imaging algorithms for 2D and 3D images (ROY et al., 2016) (STOTZKA et al., 2002) (WAAG; FEDEWA, 2006).

A prototype under development by the Karlsruhe Institute of Technology in Germany is a semi-elliptical tank filled with water where the breast is dipped in and it has 157 multi-element transducers attached to its wall. Each of these transducers has 4 dedicated elements to emit waves at the center frequency of 2.4 MHz, and 9 dedicated elements to receive, resulting in a total of 628 emitters and 1413 receivers (GEMMEKE et al., 2017).

Delphinus Medical Technologies is also developing a breast UST system called SoftVue®. This device has 2048 single-element transducers that operate at a center frequency of 3 MHz and are distributed in the form of a ring. In the case of SoftVue®, the ring moves vertically, with a 2 mm step, to collect the data for reconstruction of 3D images (DURIC et al., 2013).

Despite applications in breast imaging, UST has never been used to monitor the lungs because it is a very challenging task. During the inspiration, the lungs would be full of air, and it represents a high attenuation medium for ultrasound waves. However, Rueter et al. (2010) showed that, for non-invasive lung monitoring, an ultrasound wave with central frequency lower than 750 kHz would be able to pass through the entire thoracic wall.

Recently, Song et al. (2018) also showed that it is feasible to use low frequency ultrasound for human thorax imaging. Hence, UST could be a new method for continuous non-invasive lung imaging of mechanically ventilated patients in ICUs.

In order to develop a novel UST system for lung monitoring, both hardware and software must be researched. The hardware is composed of transducers, their drivers, and an acquisition system while the software is composed of beam forming algorithms and imaging reconstruction algorithms (RYMARCZYK et al., 2019). In addition, the development of imaging reconstruction algorithms requires a well-known environment to estimate the imaging reconstruction error.

In the present work an experimental test bench that represents an UST system is being developed. It will be used to evaluate the feasibility of this technology as a new modality to pulmonary functional imaging, to develop the imaging reconstruction algorithms, and to understand this new technology for the development of UST for clinical applications.

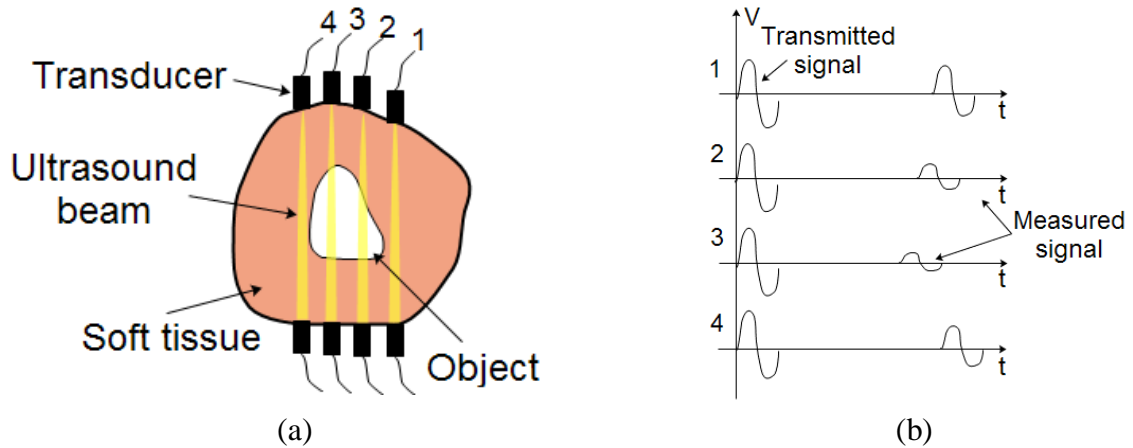
2 BACKGROUND

Tomography is a technique used to create cross-sectional imaging of an object. It has been widely applied in medical field, for both anatomical and functional imaging in different exam modalities such as CT, UST and EIT, for diagnosis and assessments of patients. This technique allows the creation of high resolution images (CT) for identification of internal structures of organs, as well as continuous and real-time images (EIT) for monitoring of some functions of organs.

Since UST is based on ultrasound waves, transmission and reflection algorithms can be applied to image an object. Transmission algorithms are based on attenuation and speed of sound of ultrasound waves, which requires a transmitting and receiving ultrasound transducer. This technique provides information about the tissue of the object that is imaged. Meanwhile, Reflection algorithms use the reflection properties of ultrasound waves, providing information about the object boundaries. To apply this technique, an ultrasound transducer operates both as transmitter and receiver. Both transmission and reflection techniques can be combined to improve the imaging quality, and provide more information about the object that is being imaged.

To make cross-sectional images using the refractive index, it must be considered that the central frequency of the transducer is high enough so that the ultrasound beam divergence angle can be neglected, resulting in a high spatial resolution, and that the speed of sound in soft tissue is close to the speed of sound in water, which is about 1500 m/s (KAK; SLANEY, 2001). This method is mainly based on the time delay and the path of each transmitted ultrasound wave. Figure 1A shows 8 transducers (4 transmitters + 4 Receivers), for each received signal, there is a different time of flight that can be seen in Figure 1B. Thus, this information is used to create images.

Figure 1: Time of flight of 4 transmitted ultrasound waves.



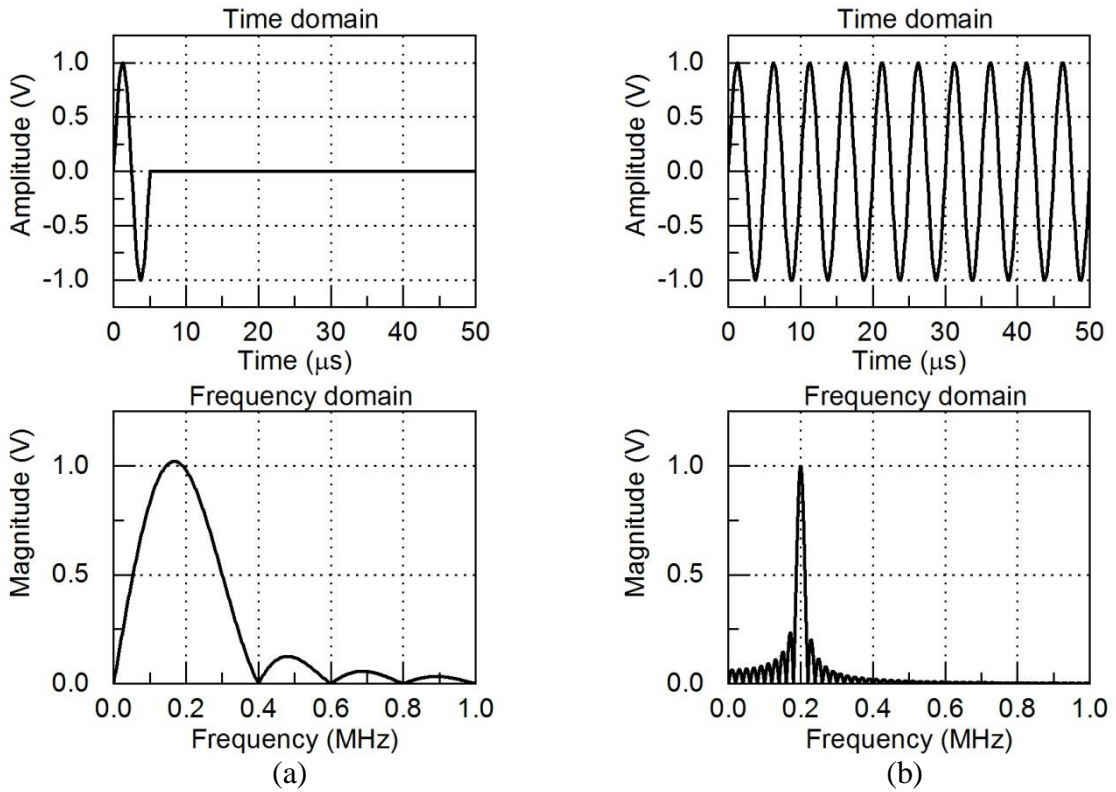
Source: Author.

Another method to create cross-sectional imaging using ultrasound is through the attenuation coefficient. Different from the refractive index, the attenuation coefficient method is a function of frequency at any point in the cross-section plane. Moreover, this method also requires that the transmitted pulse has most of its energy concentrated in a single frequency. Consequently, the transducer must be driven by a pulsed Continuous Wave (CW) signal, which means that a long burst signal must be used to guarantee that the transducer response will surpass the transient (KAK; SLANEY, 2001).

There are at least three techniques to determine the attenuation coefficient: Energy Ratio Method, Division of transforms Followed by Averaging Method and Frequency-Shift method. The first two methods are based on the transfer function of the tissue structure along the ultrasound beam, which depends on the Fourier Transforms of signals that are measured only with water and signals that pass through the tissues. For the Frequency-shift method, the difference is that instead of determining the transfer function, it is calculated the central frequency of both signals (KAK; SLANEY, 2001).

Figure 2 illustrates the differences between the time and frequency domain of signals that have different amount of cycles. It can be seen that for a 200 kHz sinusoidal pulse the bandwidth is wider than for a 10-cycle sinusoidal burst with the same central frequency. Therefore, it shows that it is necessary a certain amount of pulses to concentrate the energy in a single frequency so that the attenuation coefficient can be determined (KAK; SLANEY, 2001).

Figure 2: Time and frequency domain of sinusoidal pulses. (a) 1 pulse and (b) 10 pulses.



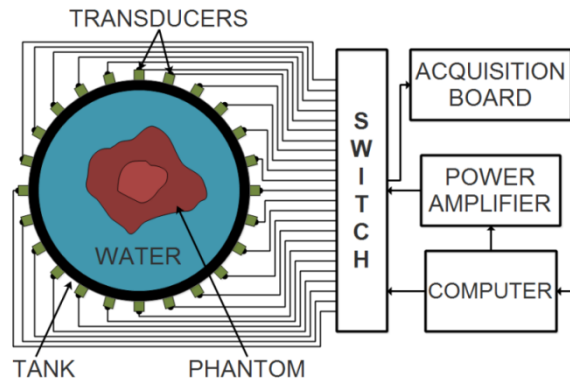
Source: Author.

Depending on the body region that is desired to be imaged, transmission techniques may not be possible to reconstruct images. Thus, an alternative is to create imaging algorithms that use ultrasound wave reflections, which is commonly used in conventional ultrasound.

Different from the transmission techniques, in which can be used both narrow and broadband transducers, the reflection tomography requires only broadband transducers because it is necessary higher spatial resolution to identify the tissue layers. Therefore, each transducer operates as transmitter and receiver, and since the transducer only transmits short time pulses, the received signals will contain all reflections from tissues interfaces (KAK; SLANEY, 2001).

To develop reconstruction imaging algorithms, prototype systems are required so that it can provide a well-known environment, which is used to better understand the inverse problem and define parameters for algorithms. Having a robust prototype system for UST is important because reconstruction imaging algorithms cannot be tested and evaluated without enough data from the object that is desired to be imaged. Figure 3 illustrates the components that are used to design a prototype system for UST (SONG et al., 2017).

Figure 3: Overview of a prototype system for developing reconstruction imaging algorithms of UST.



Source: Author.

The ultrasound transducers are fixed on the cylindrical tank wall in order to create a ring array. The central frequency of transducers and whether it is single-elements or multi-elements are determined by the application.

Since the speed of sound in water is approximately the same as in soft tissues, it works as a propagation medium and a coupling interface between the phantom and the ultrasound transducers. In addition, a phantom is used to mimic the acoustic properties of biological tissues.

A Switch selects which transducer is an emitter or receiver so that both transmission and reflection techniques can be used. A power amplifier drives the transducers while the acquisition board records the captured signals and transfers it to the computer, in which the recorded data is processed and used in the reconstruction imaging algorithms.

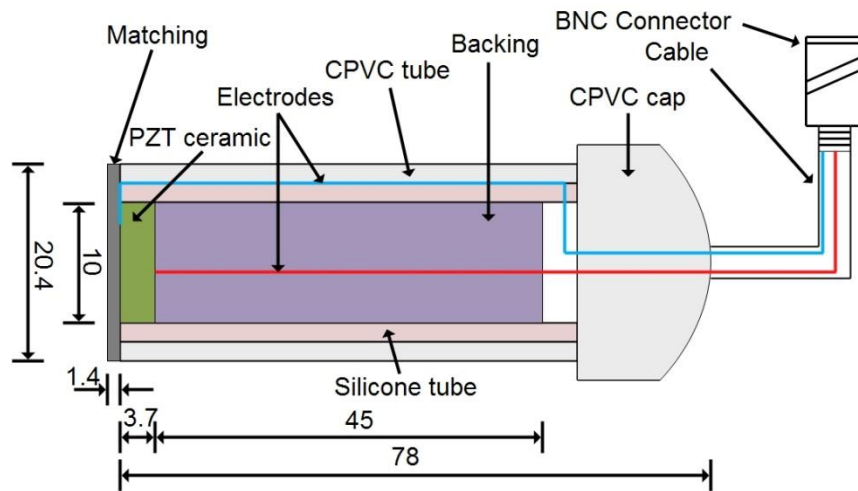
3 MATERIALS AND METHODS

In the development of a test bench for UST, different stages are performed, which include: the manufacturing and the characterization of ultrasound transducers, and the design, the manufacturing and the evaluation of the test bench.

3.1 PZT ultrasound transducer

Figure 4 illustrates a schematic of a single element transducer. A Lead Zirconate Titanate (PZT) ceramic, (DL50, Delpiezo Inc., U.S.A.) with resonance frequency of 500 kHz, is placed inside of a silicone tube to avoid short circuit between both electrodes, and then a backing layer mixture is poured into the silicone tube on the backside of the PZT ceramic.

Figure 4: PZT transducer schematic. Units in millimeters.



Source: Author.

The silicone tube is inserted into a Chlorinated Polyvinyl Chloride (CPVC) tube, which is used as the transducer housing. The electrodes are welded on both faces of the PZT ceramic and connected to a Bayonet Neill–Concelman (BNC) connector, with the red one representing the signal and blue one the ground. Silicone glue is used to fix CPVC cap to CPVC tube, and to waterproof the entire transducer.

The backing layer is used to attenuate ultrasound waves that propagate in the opposite direction to the desired one, and it can be done by mixing epoxy resin with tungsten powder. The mixture would ideally have the same acoustic impedance of the PZT ceramic, to avoid ultrasound wave reflections. However, the high concentration of tungsten would make a

homogeneous mixture impossible. Therefore, a lower concentration of tungsten was chosen in order to have a homogenized mixture.

The backing layer mixture is made from epoxy resin (SQ2001) and its hardener (SQ3154), in a ratio of 2:1 in mass. The proportion of tungsten to manufacture the backing layer is 30% in mass, which represents an attenuation of 9.13 dB/cm for a signal at 5 MHz (COELHO; PAI, 2017). Thus, considering that the sound attenuation is directly proportional to the concentration of tungsten, it results in an attenuation of 0.913 dB/cm for a signal at 500 kHz. Therefore, to guarantee a higher attenuation, the backing layer thickness is 45 mm.

An acoustic matching layer is applied on the front face of the PZT ceramic in order to transfer the maximum acoustic energy from the PZT ceramic to the desired medium. For that, the acoustic impedance of the matching layer (Z_{MAT}) must be (KINSLER et al., 2000)

$$Z_{MAT} = \sqrt{Z_{PZT} Z_{WATER}}, \quad (1)$$

with Z_{PZT} and Z_{WATER} being the acoustic impedances of the PZT ceramic and water, respectively. Therefore, for $Z_{PZT} = 23$ MRayls and $Z_{WATER} = 1.5$ MRayls, Z_{MAT} is approximately 5.7 MRayls.

The matching layer mixture is made from epoxy resin (SQ2001) and its hardener (SQ3154), in a ratio of 2:1 in mass, with 30% in volume of alumina. In addition, the thickness of the matching layer (M_{TH}) should be equal to a quarter of the wavelength of the sound wave in the mixture, so that the best coupling between the medium and the PZT ceramic occurs (KINSLER, 2000).

The thickness of the matching layer M_{TH} is defined by

$$M_{TH} = \frac{c_{MAT}}{4 \times f_{PZT}}, \quad (2)$$

with c_{MAT} as the speed of sound in the matching layer and f_{PZT} as the PZT ceramic resonance frequency. Thus, for $c_{MAT} = 2800$ m/s and $f_{PZT} = 500$ kHz, M_{TH} should be approximately 1.4 mm.

3.2 Characterization of PZT transducers

For the first version of the test bench, nine single-element transducers are manufactured in order to evaluate the manufacturing process and to assemble the test bench. However, before using these transducers, each one must be characterized so that it can provide information about the transmitted acoustic pressure, the resonance frequency and the manufacturing method. The following sessions describe the methods used to characterize our ultrasound transducers.

3.2.1 Electrical Impedance

When a transducer is manufactured, both mechanical and electrical properties change according to the housing material, matching and backing layers, wiring, and connectors. Thus, these factors affect the resonance frequency of the manufactured transducer.

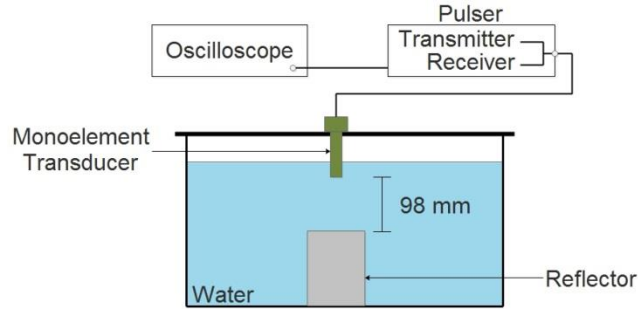
These manufacturing effects can be seen through the electrical impedance response, which means that the resonance frequencies and vibration modes of each transducer can be estimated based on its electrical impedance. Therefore, the electrical impedances of the PZT ceramics are measured by an impedance analyzer (4294A, Agilent, USA) and compared to the ones of the manufactured transducers.

3.2.2 Pulse-Echo technique

Figure 5 shows a schematic for the application of the pulse echo technique. Each manufactured transducer was immersed in a water tank with a reflector positioned at a distance of 98 mm from the transducer. Moreover, the dimensions of the tank are large enough to guarantee that there is no interference from signals reflected from the tank wall.

A Pulser (5077PR, Olympus, Japan) drives the transducer with a square wave (amplitude of 100 V, pulse width of 4 μ s and repetition time of 10 ms); the receiver gain was set at 0 decibel (dB). Then, each echo signal was recorded by an oscilloscope (DSO3102A, Agilent, USA) and processed in MATLAB to obtain the maximum peak-to-peak amplitude (V_{PP}) and the resonance frequency.

Figure 5: Schematic for the pulse-echo technique.



Source: Author.

3.2.3 Resonance frequencies

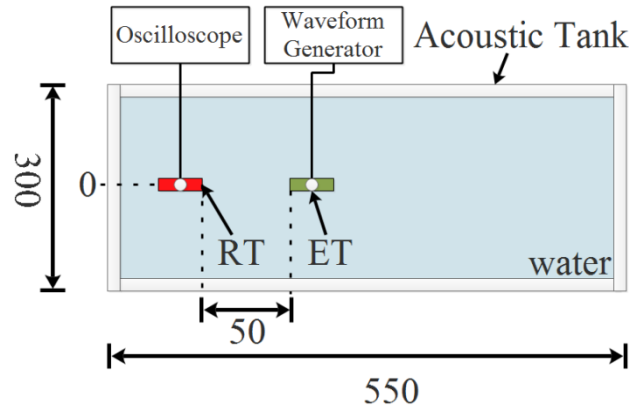
The electrical impedance measurements provide information about the frequency interval (f_i) that includes the resonance frequency (f_R) of each transducer. Thus, by varying the frequency of the signal that drives the manufactured transducers within f_i , it can be used to determine f_R , which is given by the highest amplitude of the captured signal.

Determining f_R is important because to transmit the maximum acoustic pressure, each transducer must be driven by its resonance frequency. However, it is likely that each transducer has a different f_R . Therefore, after measuring the f_R of all transducers, a central resonance frequency (f_C) is chosen to have the same general frequency to drive all transducers.

Figure 6 shows a schematic for the transmitting-receiving measurements in which the Emitting Transducer (ET) and Receiving Transducer (RT) are placed inside an acoustic tank filled with deionized water at a distance of 50 mm from each other. Moreover, the figure also shows the acoustic tank dimensions, which are great enough to avoid interference from the acoustic tank wall. The acoustic tank has 150 mm in height, and the transducers were positioned at 75 mm. An oscilloscope (MSOX2004A, Keysight, USA) was used to measure the signals, while a waveform generator (AFG1062, Tektronix, USA) was used to drive the transducers. Moreover, the dimensions of the acoustic tank do not influence on the captured signal during the measurements.

Each of the nine transducers is driven by a sinusoidal pulse of 20 V_{PP} in amplitude and frequency f_R while an oscilloscope records the captured signals from the other eight transducers. Moreover, the recorded signals are processed in Matlab to determine the signal attenuation when driving the manufactured transducers with different frequencies than f_R .

Figure 6: Top view of the schematic for measuring f_R . Units in millimeters.



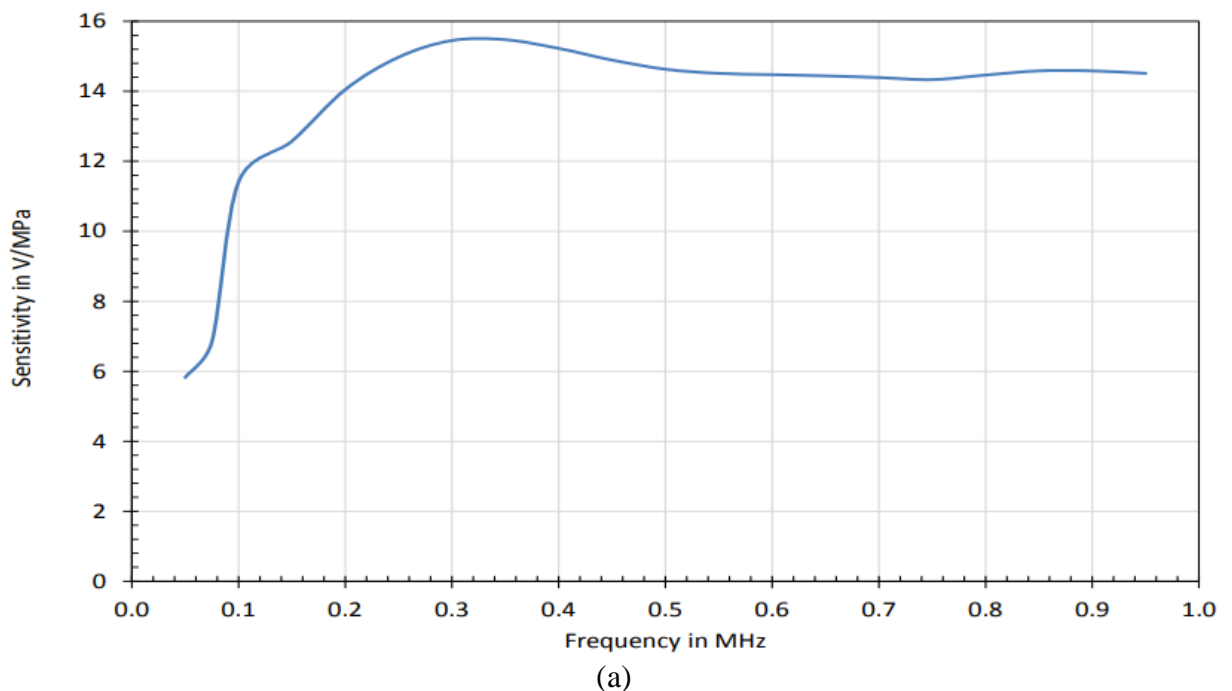
Source: Author.

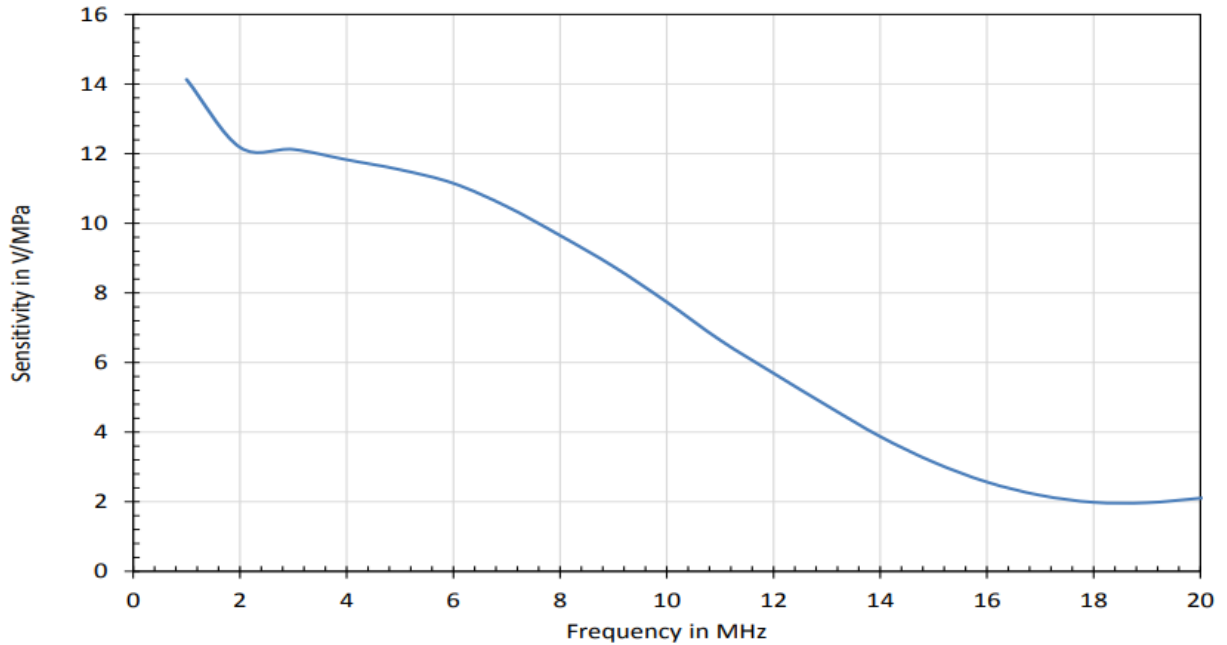
3.2.4 Acoustic Pressure

The method that is applied to convert the measured signals (volts) into acoustic pressure (Pascal) is through the sensitivity of calibrated hydrophones. For all acoustic pressure measurements, it is used a 4.0 mm needle hydrophone (NH4000, Precision Acoustics, UK).

Figure 7 shows the sensitivity response of the hydrophone from 30 kHz to 20 MHz. It can be seen that from 30 kHz to 400 kHz, the sensitivity response is not flat. This can bring some inaccuracies when measuring signals with frequencies below 400 kHz.

Figure 7: Sensitivity response of the hydrophone: (a) from 30 kHz to 1 MHz (b) 1 MHz to 20 MHz.





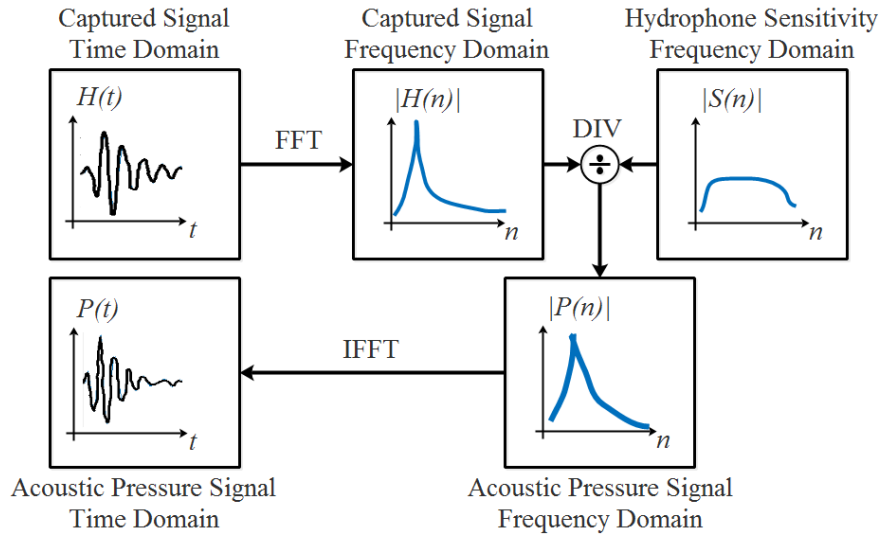
(b)

Source: (NH4000, Precision Acoustics, UK).

When driving transducers with short pulses, the captured signals are composed by the sum of several frequencies. Moreover, these signals may also have harmonic content because of different driving signals, making it difficult to select only a single frequency to calculate the acoustic pressure.

Figure 8 illustrates a method to calculate the acoustic pressure by compensating the regions that the sensitivity response is not flat. Using Matlab, the captured signal frequency response is calculated by the Fast Fourier Transform (FFT) so that all coefficients can be divided by the hydrophone sensitivity according to its frequency, resulting in acoustic pressure that has the same bandwidth from the captured signal. The sensitivity response was defined in Matlab by using Figure 7.

Figure 8: Block diagram to calculate the acoustic pressure.



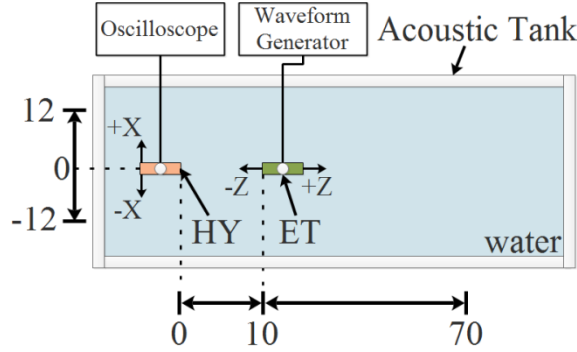
Source: Author.

Although the frequency resolution of the sensitivity may be different from FFT frequency resolution, a linear interpolation is applied on the hydrophone sensitivity response to match the number of points of both functions to guarantee that these functions have the same frequency resolution. Therefore, after having the acoustic pressure coefficients, it is applied the Inverse Fast Fourier Transform (IFFT) to have the acoustic pressure signal in the time domain, which is used to calculate the peak-to-peak acoustic pressure.

3.2.4.1 Sinusoidal pulse

Figure 9 illustrates the schematic for measuring the acoustic pressure transmitted by the manufactured transducers. A waveform generator is used to create a sinusoidal pulse of $20 V_{PP}$ in amplitude and central frequency given by f_C . The calibrated needle hydrophone (HY) is used to capture the emitted signals from the nine ETs, and then the measurements are processed in Matlab to convert it into acoustic pressure. Moreover, the dimensions of the acoustic tank are the same as in Figure 6 and do not influence on the captured signal during the measurements.

Figure 9: Top view of the acoustic tank for measuring the acoustic pressure using a sinusoidal pulse. Units in millimeters.



Source: Author.

To determine the acoustic map dimensions, a preliminary measurement was done to evaluate the distances in X and Z axis that covers the acoustic pressure distribution. Hence, for all the measurements, the acoustic map dimension is [-12, 12] mm in X axis and [10, 70] mm in Z axis. The spatial resolution must be at least half of the wavelength in water (λ_{WATER}), which is given by

$$\lambda_{WATER} = \frac{c_{WATER}}{f_C}, \quad (3)$$

with c_{WATER} the speed of sound in water, to ensure that there will not be loss of information due to aliasing. For signals with central frequency equals to 170 kHz, the λ_{WATER} is equal to 8.8 mm. Thus, this information can be used to choose the spatial resolution when mapping the acoustic field.

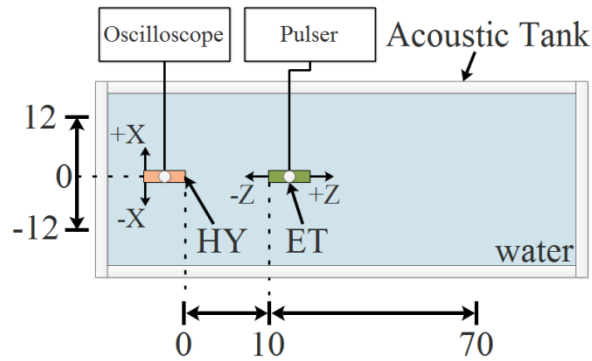
3.2.4.2 Square pulse

Since the mean thoracic diameter is around 30 cm and the lungs represent a high attenuation medium for ultrasound waves, a higher acoustic pressure may be needed in order to have enough energy to be captured by the manufactured transducers.

The waveform generator can only provide signals with maximum amplitude of 10 V. Thus, a Pulser (5077PR, Olympus, Japan) is also used to drive the transducers with a 100 V_{PP} square pulse and pulse width (P_{WD}) around $1/(2 \times f_C)$.

Figure 10 illustrates a schematic for measuring the acoustic pressure using a square pulse to drive the manufactured transducers. The method is the same from section 3.2.4.1, except for the Pulser. Thus, it allows the evaluation of which signal shape and amplitude is better to drive the manufactured transducers.

Figure 10: Top view of the acoustic tank for measuring the acoustic pressure using a square pulse. Units in millimeters.



Source: Author.

3.2.5 Transmitting-Receiving Technique

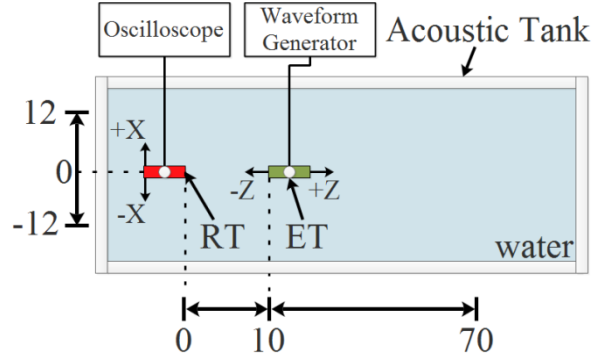
3.2.5.1 Sinusoidal pulse

Another important parameter that shows how good a transducer is when operating as a RT is its sensitivity, which gives information about the conversion of acoustic pressure into voltage.

Once having the acoustic pressure distributions, these measurements can be used to estimate the sensitivity of each transducer. For that, an ET must be used as a known acoustic pressure source while the other transducers operate as RTs. It guarantees that the same acoustic pressure is applied to all transducers so that the amplitude differences of each captured signal are given by the sensitivity.

Figure 11 shows the schematic to capture signals using eight transducers as RTs while an ET is driven by a sinusoidal pulse of 20 V_{PP} in amplitude and central frequency f_C . The acoustic map dimensions are the same from the 3.2.4.1 section for comparison purpose.

Figure 11: Top view of the acoustic tank with a waveform generator and measuring with RTs. Units in millimeters.



Source: Author.

To calculate the estimated sensitivity (S) when driving a transducer with sinusoidal pulse, the following expression is applied

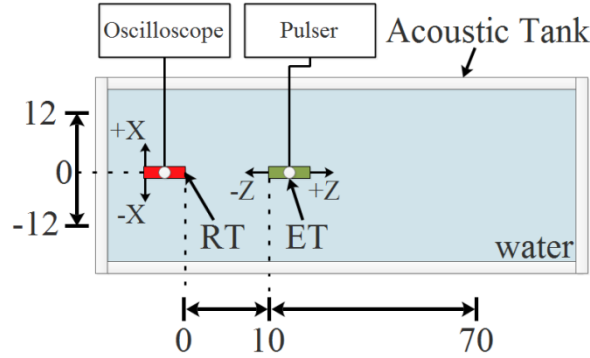
$$S = \frac{CS|_{X=0mm, Z=10mm}}{AP|_{X=0mm, Z=10mm}} \times 10^6 \text{ V/MPa.} \quad (4)$$

CS is the captured signal by a RT and AP is the measured acoustic pressure generated by the ET, with both signals measured at $X = 0$ mm and $Z = 10$ mm.

3.2.5.2 Square pulse

Following the same procedure presented in section 3.2.5.1, Figure 12 shows the schematic to capture signals with 8 RTs when driving an ET with a 100 V_{PP} square pulse and P_{WD} . Moreover, the sensitivities of the manufactured transducers are also estimated when driving the ET with a square pulse signal using the same expression showed in Eq. (4).

Figure 12: Top view of the acoustic tank with a Pulser and measuring with RTs.



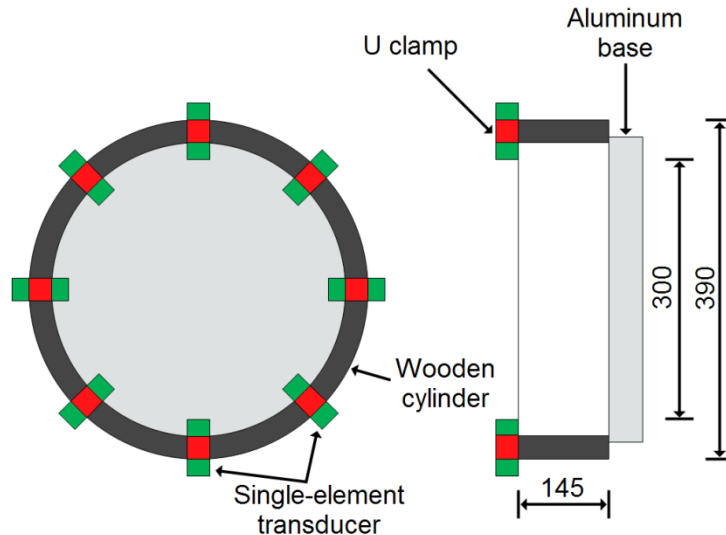
Source: Author.

3.3 Manufacturing and assembly of the test bench

Figure 13 shows a schematic of a first version of the UST test bench. It consists of a wooden cylinder on which 8 single-element PZT transducers are fixed. The manufactured transducers are equidistantly attached on the wooden cylinder by U clamps.

The distance between the front face of two transducers is 300 mm, which is the mean diameter of the human thorax. The wooden cylinder is waterproofed by wood sealer and marine varnish, and fixed on an aluminum base.

Figure 13: Schematic of the test bench. Units in millimeters.



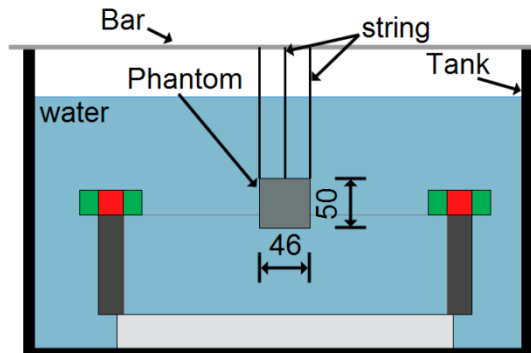
Source: Author.

To capture the signals using a UST configuration, the test bench is placed in an acoustic tank filled with water, as shown in Figure 14. Thus, while a transducer transmits

ultrasound signals, the other seven transducers capture the ultrasound signals after passing through the medium.

A cylindrical phantom mold was designed by using Polyvinyl Chloride (PVC) tube as wall and a glass plate as base. The phantom is made from a mixture of epoxy resin (ARALDITE GY 260) and 20% in volume of its hardener (ARADUR HY 956), and it was placed between transducers by using strings, which are fixed on a bar placed on the top side of the tank. Therefore, the phantom could be placed in different positions inside the test bench.

Figure 14: Test bench placed in a tank filled with water. Units in millimeters.



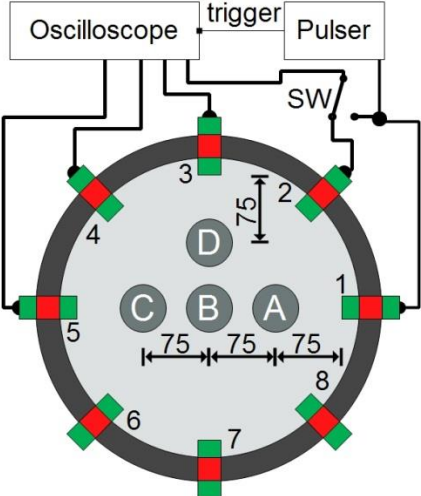
Source: Author.

3.4 Evaluation of the test bench

Figure 15 illustrates the assembly of the test bench with 8 single-element transducers attached to its wall. The phantom was placed in four positions (A to D) so that different signals could be recorded and analyzed. Only transducers (T2 to T5) were used to capture the signals because it is enough to show if changes in the phantom position can be detected.

A Pulser (5077PR, Olympus, Japan) generated a trigger signal to synchronize the oscilloscope (MSO8104A, Agilent, USA) and drove the Transducer 1 (T1) with a square pulse of 100 V_{PP} in amplitude, width of 2.8 μ s, and repetition time of 10 ms, whereas the oscilloscope recorded the signals that were received by the other transducers. In the Figure 15, SW represents a connection of the oscilloscope channel that is used to record the pulsed signal that drives T1, or the signal captured by Transducer 2 (T2).

Figure 15: Schematic of the complete system to transmit and receive signals for UST. Units in millimeters.



Source: Author.

4 RESULTS AND DISCUSSIONS

4.1 PZT ultrasound transducer

Before manufacturing the transducers, a dummy was made in order to evaluate whether the housing would waterproof the transducers. Thus, after three hours in water, the dummy showed no leaking and proved to be waterproof.

Figure 16 shows the manufactured PZT ultrasound transducer and its dimensions. 9 single-element transducers were manufactured with all of them having almost the same dimensions.

Figure 16: Manufactured single-element PZT ultrasound transducer. Units in millimeters.



Source: Author.

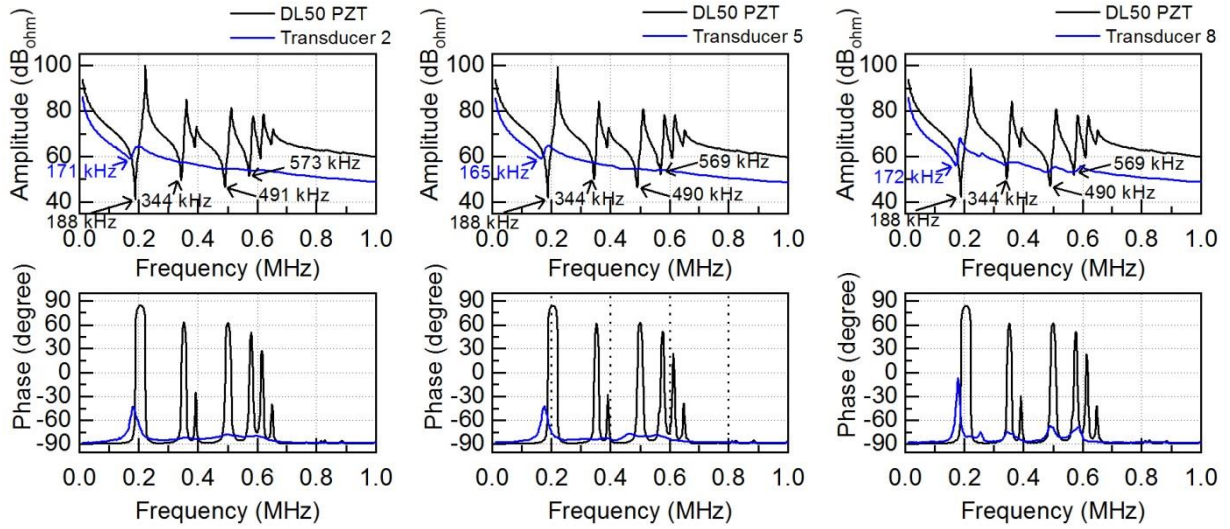
4.2 Characterization Results

4.2.1 Electrical impedance

Figure 17 shows the electrical impedance of the DL50 PZT ceramics and the final electrical impedance of 3 manufactured transducers. The measured amplitude in ohm of the

electrical impedances were divided by 1 and converted to dB. All other manufactured transducers have similar electrical impedance measurement.

Figure 17: Electrical impedance of PZT ceramic and manufactured transducers. (a) Transducer 2, (b) Transducer 5 and (c) Transducer 8



(a)

(b)

(c)

Source: Author.

Comparing the electrical impedances of transducer 2 and DL50 ceramic, the PZT ceramic contains other resonance frequencies, 188 kHz, 344 kHz, and 573 kHz, with the axial resonance frequency as 491 kHz. These other resonance frequencies are related to other vibration modes, which are given by the PZT ceramic geometry, depending on its thickness and diameter.

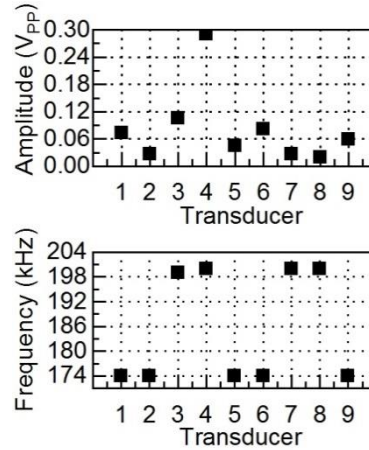
Due to the fact that the ratio (diameter/thickness) of the PZT ceramic is lower than 20, the radial mode (188 kHz) is more predominant than the axial mode of vibration (491 kHz) (KUNKEL; LOCKE; PIKEROEN, 1990). Thus, analyzing the electrical impedance of transducer 2, only the low frequency vibration mode at 171 kHz is visible, and the same occurs to the other transducers. Moreover, this effect cannot be avoided without changing the geometry of the PZT ceramic or boundary conditions.

4.2.2 Pulse-echo technique

Figure 18 illustrates the maximum amplitude V_{PP} and resonance frequency of the manufactured transducers. Each transducer has its amplitude signal different from other

transducers, with transducer 4 presenting the highest difference. It happened because of the manufacturing process of the backing and matching layers.

Figure 18: The maximum amplitude (V_{PP}) and resonance frequency of each transducer manufactured.



Source: Author.

The mixtures of the backing and matching layers were not well-homogenized, influencing directly on the transducer responses. Another problem is that the proportion of alumina used to make the matching mixture is high in ratio with epoxy resin, resulting in a dense paste. Hence, it is extremely difficult to homogenize the mixture and to remove all the bobbles during the mixing process.

4.2.3 Resonance frequencies

The electrical impedance measurements also show that the resonance frequencies of the manufactured transducers are within a $f_i = [150-200]$ kHz. Therefore, the corresponding signals to 150 kHz, f_R and 200 kHz were captured using an ET and eight RTs each time, resulting in a total of 3×72 measurements.

Table 1 shows the f_R of each transducer, which was measured using an oscilloscope, and Table 2 shows its respective peak-to-peak amplitudes. In the majority of cases, f_R is equal to 170 kHz with some variations within 10 kHz. Moreover, it also proves that the electrical impedance measurements provide accurate information about f_R , despite the manufactured transducers operating in a different vibration mode. Therefore, 170 kHz was chosen as the f_C and 1 mm as the spatial resolution for all the transmitting-receiving

measurements; the blank spaces in the table are measurements that were not done due to the pandemic in 2020.

Table 1: Measured f_R for each transducer. Units in kHz.

ET \ RT	T1	T2	T3	T4	T5	T6	T7	T8	T9
T1	X	170	160	175		170	165	170	165
T2	170	X	165	170	170	170	165	170	170
T3	160	170	X	170	170	165	170	165	165
T4	165	170	170	X		170	170	165	170
T5	170	170	170	175	X	165	170	170	170
T6	170	170	170	170	165	X	170	170	
T7	165	165	170	170	170	165	X	170	170
T8	170	175	165	170	170	170	170	X	170
T9	170	165	170	170		170	170	170	X

Source: Author.

The peak-to-peak amplitudes were applied to determine the attenuation in dB of captured signals (Table 3) when driving the transducers with 150 kHz (red color) and 200 kHz (blue color) sinusoidal pulses, respectively; the blank spaces in the table are measurements that were not done due to the pandemic in 2020.

Table 2: Peak-to-peak amplitudes of captured signals for driving transducer with a sinusoidal pulse. Units in V_{pp} .

ET \ RT	T1	T2	T3	T4	T5	T6	T7	T8	T9
T1	X	0.21	0.34	0.23		0.27	0.41	0.31	0.32
T2	0.15	X	0.17	0.12	0.08	0.12	0.17	0.14	0.14
T3	0.36	0.20	X	0.23	0.16	0.26	0.38	0.29	0.31
T4	0.32	0.18	0.31	X		0.24	0.37	0.29	0.18
T5	0.15	0.08	0.12	0.05	X	0.07	0.18	0.11	0.08
T6	0.26	0.14	0.24	0.17	0.12	X	0.30	0.22	
T7	0.44	0.24	0.40	0.30	0.19	0.32	X	0.21	0.37
T8	0.32	0.18	0.28	0.13	0.13	0.24	0.36	X	0.22
T9	0.22	0.16	0.20	0.21		0.16	0.25	0.12	X

Source: Author.

Since power amplifiers are based on clock frequency and the higher is the frequency resolution the more expensive is the chipset, driving the manufactured transducers with a 170 kHz signal may not be possible. Therefore, the attenuation coefficients show estimation for the losses when driving the manufactured transducers with different frequencies.

All attenuation coefficients are higher than -0.9 dB, which leads to losses smaller than 10 %. Thus, driving the manufactured transducers with frequencies from 150 to 200 kHz, it would not result in high losses to the system; the blank spaces in the table are measurements that were not done due to the pandemic in 2020.

Table 3: Attenuation coefficients for driving transducers with 150 kHz (red color) and 200 kHz (blue color) sinusoidal pulse. Units in dB.

ET \ RT	T1	T2	T3	T4	T5	T6	T7	T8	T9
1	X	-0.256	-0.16	-0.48		-0.17	-0.17	-0.23	-0.17
T2	-0.24		-0.29	-0.54	-0.52	-0.33	-0.26	-0.31	-0.27
T3	-0.36	X	-0.61	-0.21	-0.27	-0.50	-0.45	-0.22	-0.49
T4	-0.12	-0.29		-0.58	-0.45	-0.15	-0.19	-0.14	-0.25
T5	-0.63	-0.59	X	-0.41	-0.61	-0.53	-0.60	-0.51	-0.69
T6	-0.08	-0.31	-0.24			-0.12	-0.24	-0.24	-0.43
T7	-0.37	-0.50	-0.71	X		-0.46	-0.45	-0.51	-0.37
T8	-0.20	-0.30	-0.57	-0.73		-0.18	-0.33	-0.47	-0.49
T9	-0.29	-0.62	-0.74	-0.33	X	-0.25	-0.35	-0.45	-0.85
T2	-0.11	-0.36	-0.19	-0.24	-0.15		-0.19	-0.30	
T3	-0.45	-0.43	-0.50	-0.40	-0.50	X	-0.52	-0.43	
T4	-0.16	-0.31	-0.21	-0.48	-0.42	-0.18		-0.30	-0.29
T5	-0.60	-0.55	-0.54	-0.48	-0.48	-0.51	X	-0.55	-0.47
T6	-0.36	-0.39	-0.21	-0.35	-0.34	-0.21			-0.15
T7	-0.53	-0.50	-0.53	-0.20	-0.33	-0.58	-0.40	X	-0.46
T8	-0.36	-0.19	-0.23	-0.37			-0.38	-0.50	
T9	-0.48	-0.18	-0.20	-0.28		-0.09	-0.30	-0.34	X

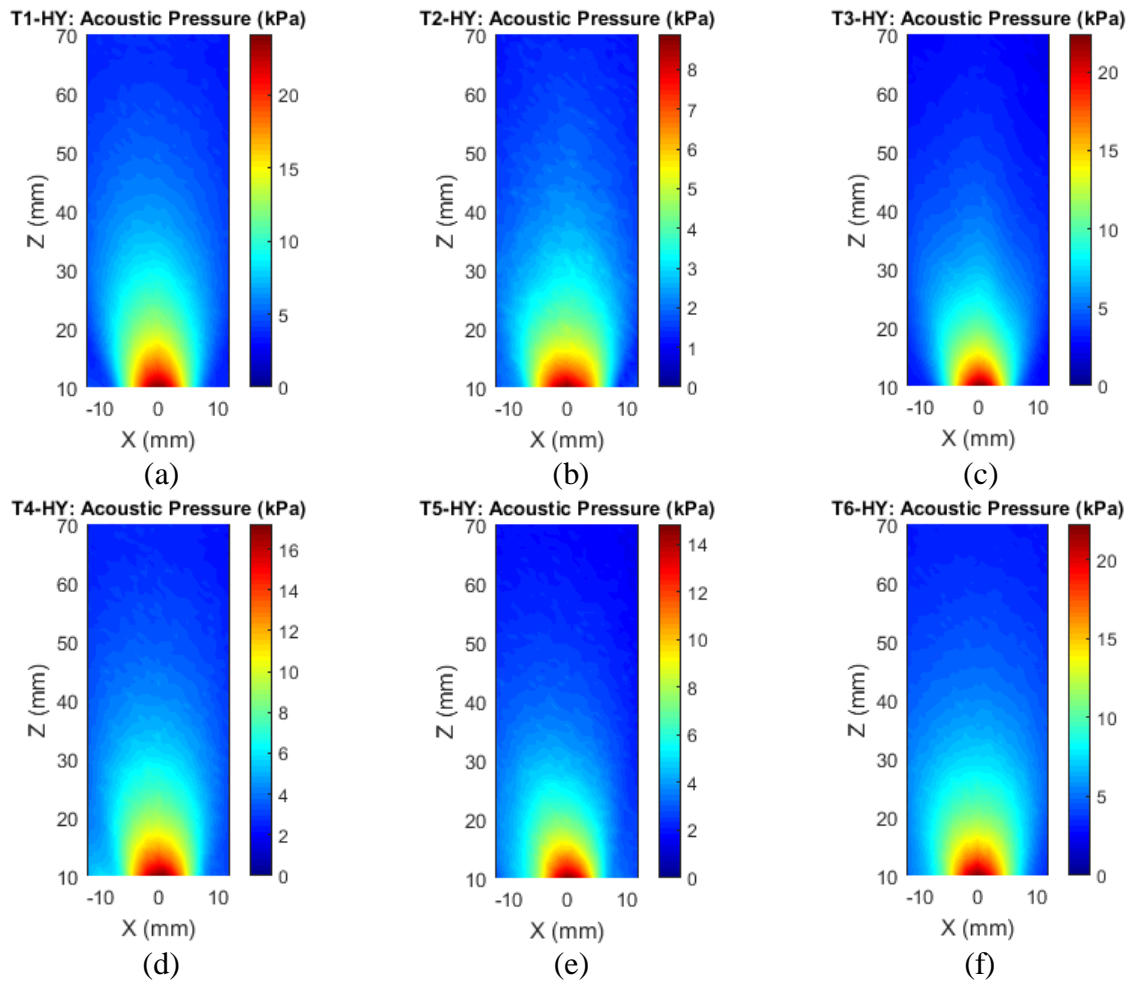
Source: Author.

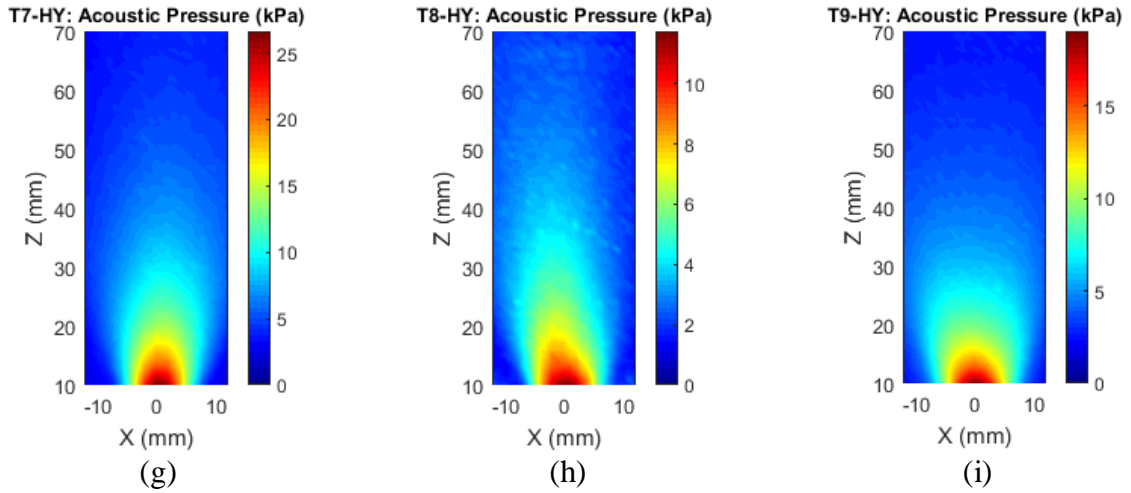
4.2.4 Acoustic Pressures

4.2.4.1 Sinusoidal pulse

Figure 19 shows the measured acoustic pressure distributions using a hydrophone to capture signals when driving the manufactured transducers with a 170 kHz sinusoidal pulse. It can be seen that a great part of the transmitted acoustic pressure by each transducer reaches 30 mm in Z.

Figure 19: Measured acoustic pressure distribution using a hydrophone for capturing signal and a sinusoidal pulse for driving T1.

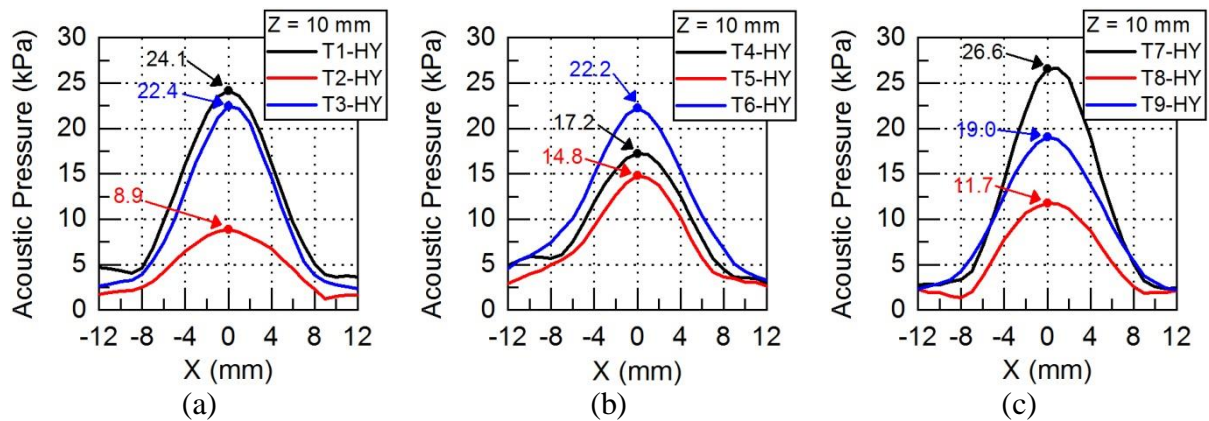




Source: Author.

Figure 20 shows the measured acoustic pressure profiles at $Z = 10$ mm for each transducer. The highest measured amplitude was given by T7 (26.6 kPa) and the lowest by T2 (8.9 kPa), which represents a difference of 66.5 %.

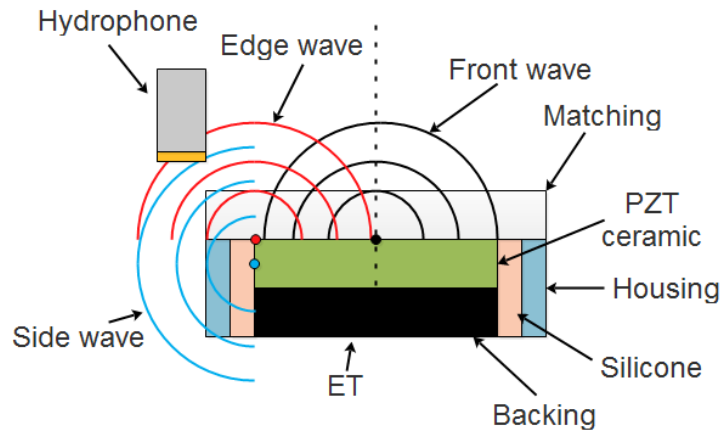
Figure 20: Measured acoustic pressure profile at $Z = 10$ mm when driving transducers with a sinusoidal pulse.



Source: Author.

For $|X| > 5$ mm, some acoustic pressure profiles present an amplitude recovery, which means that instead of decreasing, the amplitude starts to increase again. This effect could be caused by the thickness of the PZT, which is 3.7 mm. Figure 21 shows a schematic of this phenomenon. The thick PZT ceramic generated a side wave, illustrated in blue, in addition to an edge wave, illustrated in red. Thus, both waves may be interfering constructively to the measured signal.

Figure 21: Ultrasound wave propagation, ET and Hydrophone.



Source: Author.

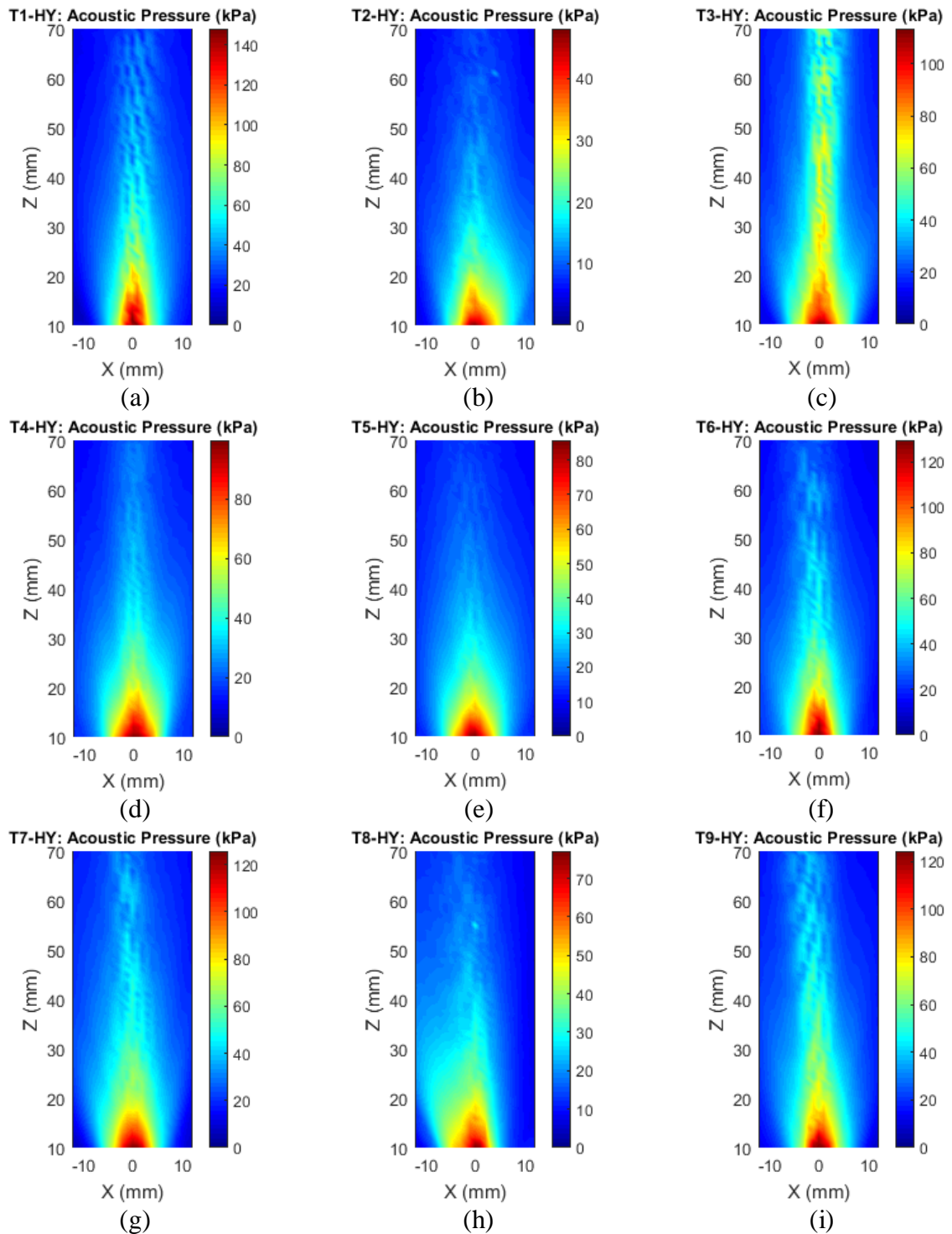
4.2.4.2 Square Pulse

Having determined the $f_c = 170 \text{ kHz}$, the P_{WD} should approximately equal to $1/(2 \times 170000) = 2.9 \mu\text{s}$. However, during practical experiments, the P_{WD} that resulted in the highest captured signal by a RT was around $2.8 \mu\text{s}$, which was the adopted P_{WD} used during the acoustic pressure and voltage measurements.

Figure 22 shows the acoustic pressure measurements when using a square pulse to drive the manufactured transducers and the hydrophone for capturing signals. For T1, T3, T4 and T7, it can be seen that the captured acoustic pressure signals have high amplitudes at $Z = 70 \text{ mm}$. However, T8 shows a bad acoustic pressure distribution, which could be a result of the square pulse source signal or manufacturing process.

The shape of the acoustic pressure distribution is narrower than the acoustic pressure distributions when driving the manufactured transducers with a sinusoidal pulse (Figure 19) which is not good for functional imaging using tomography because it is desirable that the ultrasound waves spread throughout the thorax.

Figure 22: Measured acoustic pressure distribution using a hydrophone for capturing signals and a square pulse for driving the transducers.

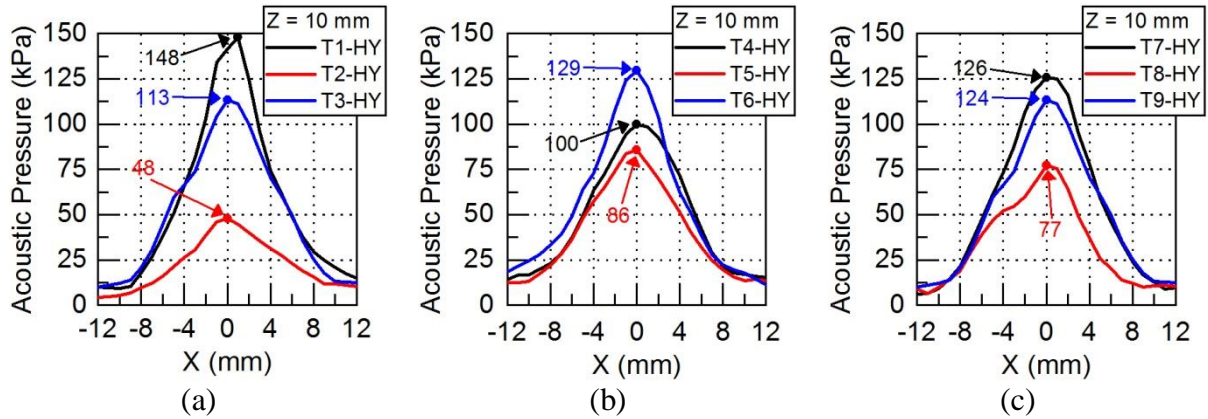


Source: Author.

Figure 23 shows the measured acoustic pressure profile at $Z = 10$ mm for each transducer. The highest measured acoustic pressure is 148 kPa whereas the smallest is 48 kPa, generated by T1 and T2 respectively, resulting in a difference of 67%.

T2 remained as the transducer which transmits the lowest acoustic energy, despite applying a different source signal. However, the highest acoustic energy is transmitted by T1, which is different from driving the transducers with a sinusoidal pulse (Figure 20).

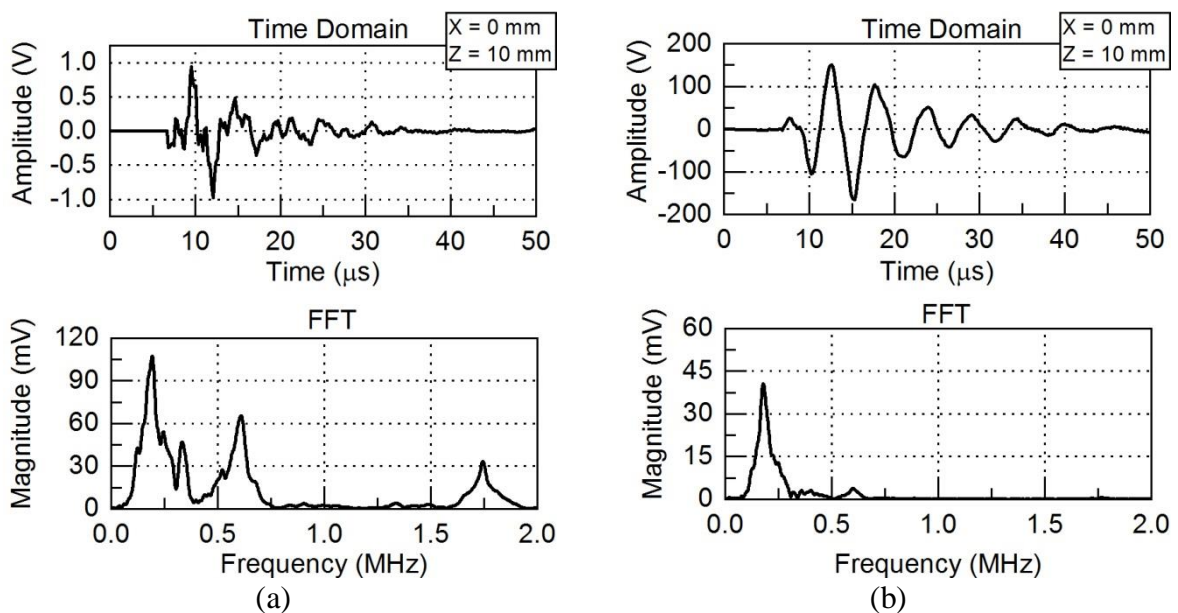
Figure 23: Measured acoustic pressure profile at $Z = 10$ mm when driving transducers with a square pulse.



Source: Author.

The differences when driving the transducers with a sinusoidal and square pulse can be seen through the FFT of the captured signal. Figure 24 shows the time domain and FFT plots of captured signals, at $X = 0$ mm and $Z = 10$ mm, using a hydrophone when driving T1 with square and sinusoidal pulses.

Figure 24: Time domain and FFT plots of acoustic pressure at $X = 0$ mm and $Z = 10$ mm. (a) Square Pulse Source and (b) Sinusoidal Pulse Source.



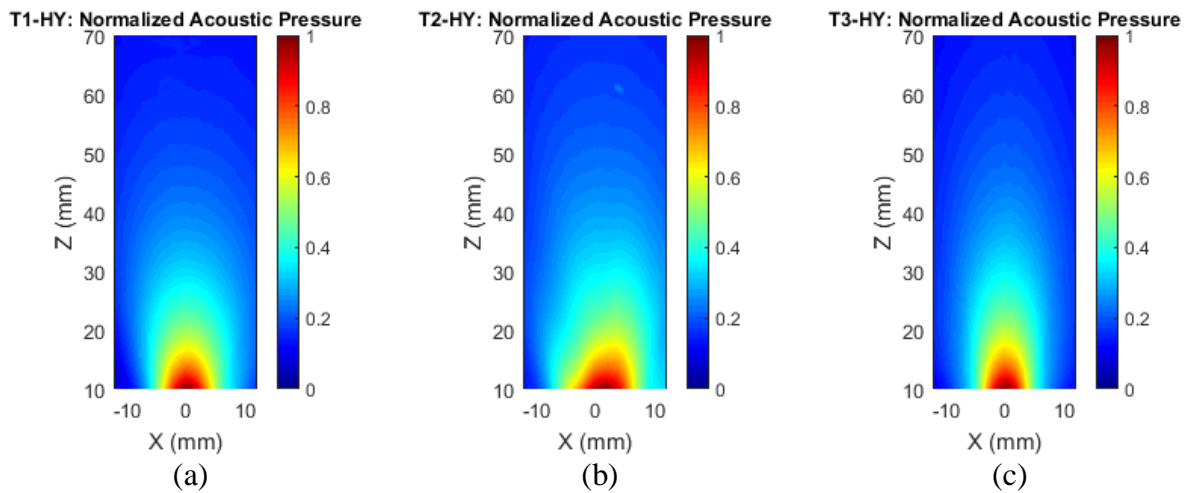
Source: Author.

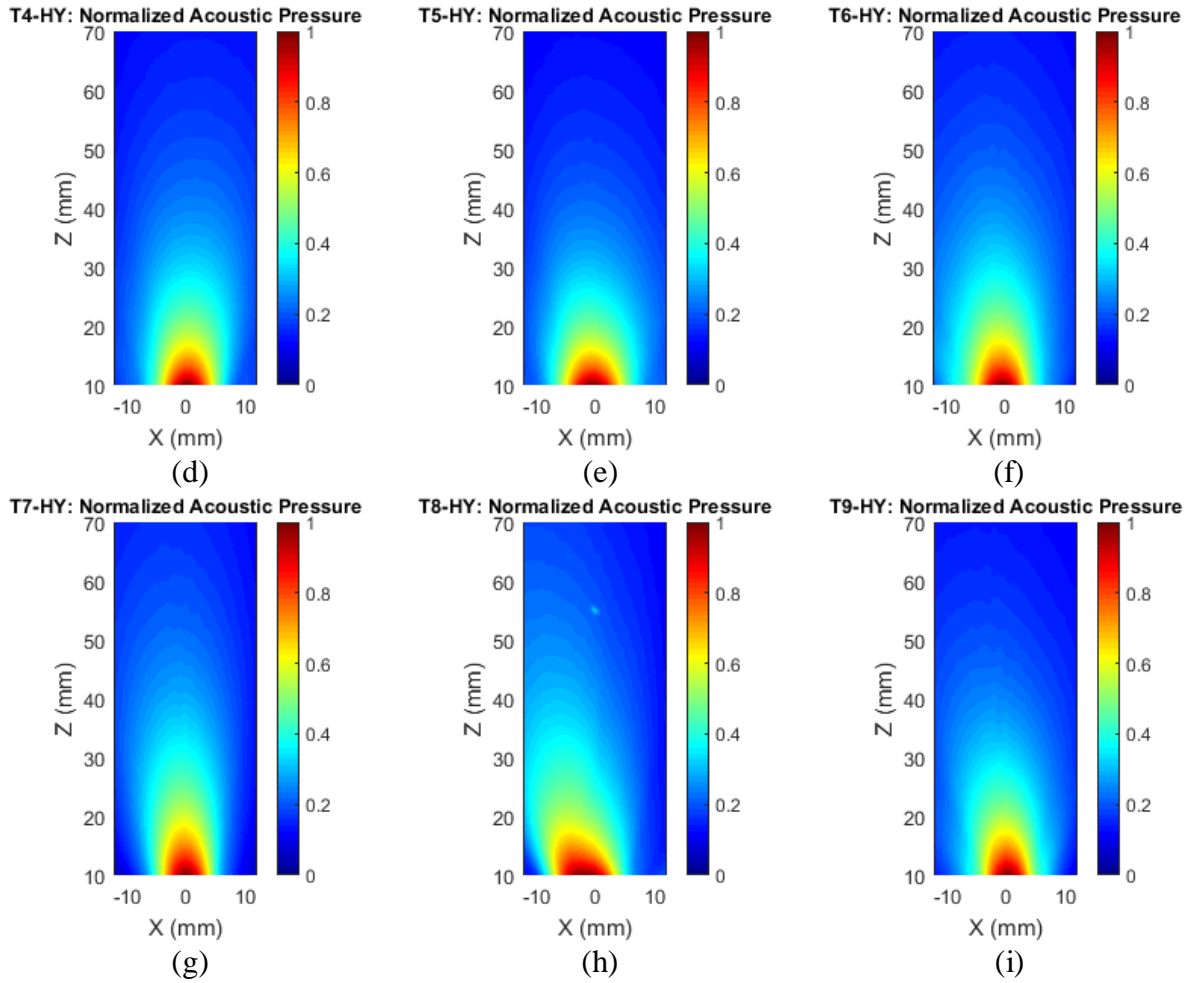
Although the amplitudes are different, it can be seen that for a square pulse source, the hydrophone captures more harmonic content compared to a sinusoidal pulse source. This effect happens because a square pulse has harmonic contents which drive the transducer with other frequencies. Moreover, since the hydrophone has a wide bandwidth, it can capture the harmonic signals.

To evaluate the influences of harmonic contents on the acoustic pressure distributions, it was selected only frequencies below 500 kHz from the captured signals showed in Figure 22, and then calculated a normalized acoustic pressure in order to visualize how the acoustic pressure distributions change.

Figure 25 shows the normalized acoustic pressure distributions for each transducer. All distributions are similar to the ones resulted by a sinusoidal pulse (Figure 19). Thus, due to the harmonic contents generated by a square pulse, it can interfere constructively and destructively in the acoustic pressure signals, resulting in narrowed distributions. Moreover, since there are high frequencies in the harmonic signal, it also indicates that there is special aliasing because of the spatial resolution is not sufficient.

Figure 25: Calculated acoustic pressure distributions for frequencies below 500 kHz using a hydrophone for capturing signals and a square pulse for driving the transducers.





Source: Author.

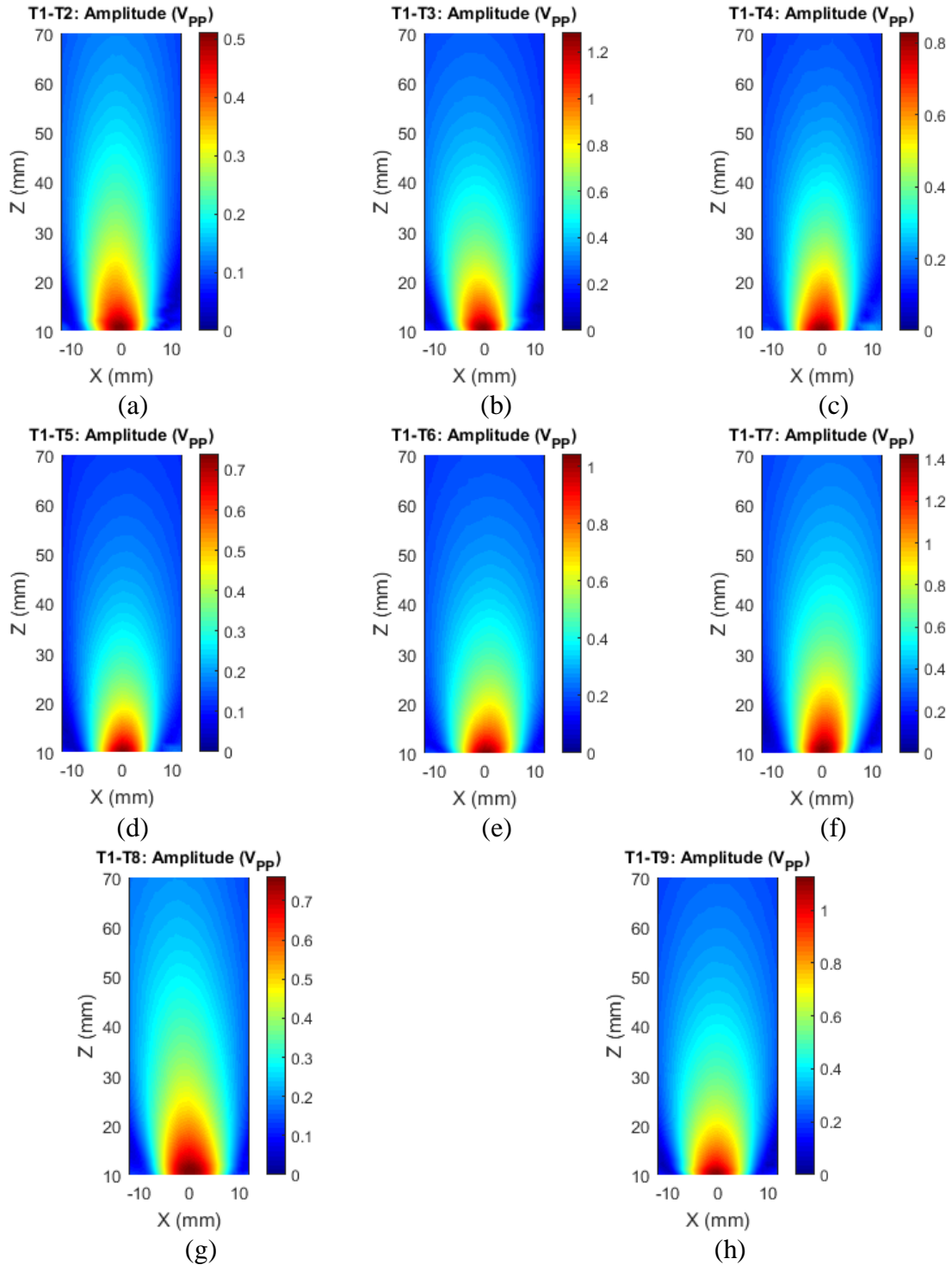
4.2.5 Transmitting-Receiving technique

4.2.5.1 Sinusoidal pulse

Figure 26 shows the measured voltage distributions when using transducers T2 to T9 as receivers and driving T1 with a sinusoidal pulse.

Different from measuring with a hydrophone, the captured signals that are spread over distances greater than $Z > 30$ mm have higher amplitudes. However, it also shows voltage amplitude differences for each transducer, confirming that the backing and matching mixtures were not well-homogenized.

Figure 26: Measured voltage distributions using transducers as receivers and driving T1 with a sinusoidal pulse.



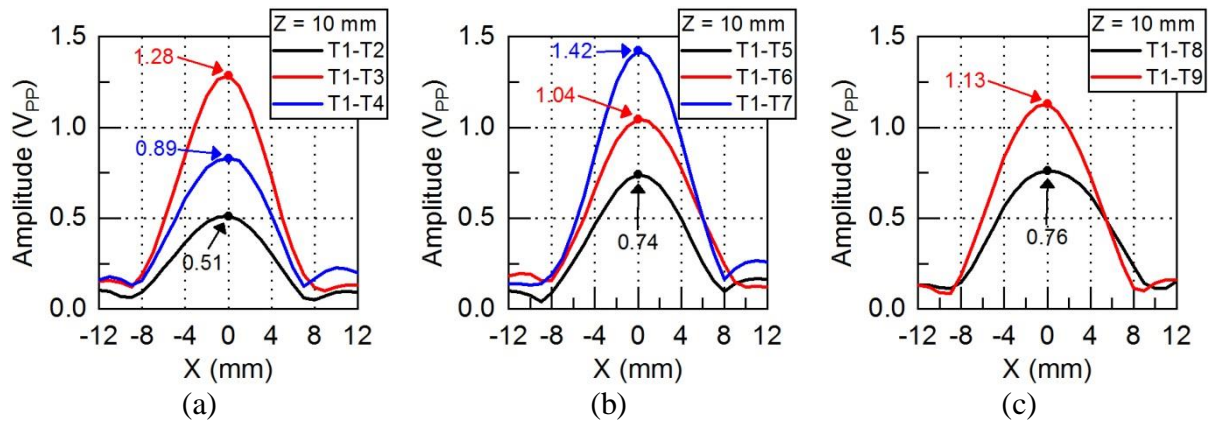
Source: Author.

At $Z = 10$ mm, the measured voltage profile of each transducer (Figure 27) presents different amplitude peaks. The highest measured amplitude is $1.42 V_{PP}$ while the smallest is $0.51 V_{PP}$, captured by T7 and T2 respectively, resulting in a difference of 64 %. Furthermore,

it can be seen that for acoustic pressure and voltage measurements, both the best ET and RT are T7 while the worst is T2.

For the acoustic pressure and voltage measurements, the difference between the highest and smallest amplitude is 66.5% and 64%, respectively. Therefore, the errors due to the manufacturing process influence both the transmitting and receiving response the same way, showing that there is a linear association between transmitting and receiving ultrasound signals.

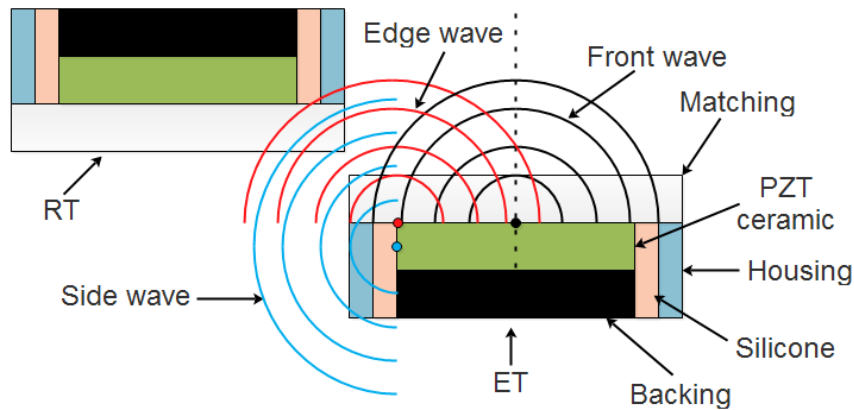
Figure 27: Measured voltage profiles at $Z = 10$ mm when receiving with transducers and driving T1 with a sinusoidal pulse.



Source: Author.

In the voltage profile graphs, the amplitude recovery effect is more visible because the thickness of PZT ceramics is also relevant when capturing signals. When it is compared to a hydrophone, the manufactured transducers have a large area of PZT ceramic, including the lateral side (Figure 28). Hence, although the RT is moving away from ET, due to the PZT ceramic thickness, a signal could still be captured, which can be the reason why there is an increasing in the amplitude response.

Figure 28: Ultrasound wave propagation, ET and RT.



Source: Author.

Table 4 shows the calculated sensitivity for T2 to T9. As expected, T7 has the highest sensitivity while T2 the smallest, 59.0 and 21.2 V/MPa respectively. Moreover, all manufactured transducers present higher sensitivities than the maximum hydrophone sensitivity, which is about 16 V/MPa.

Table 4: Calculated sensitivity when driving transducers with a sinusoidal pulse.

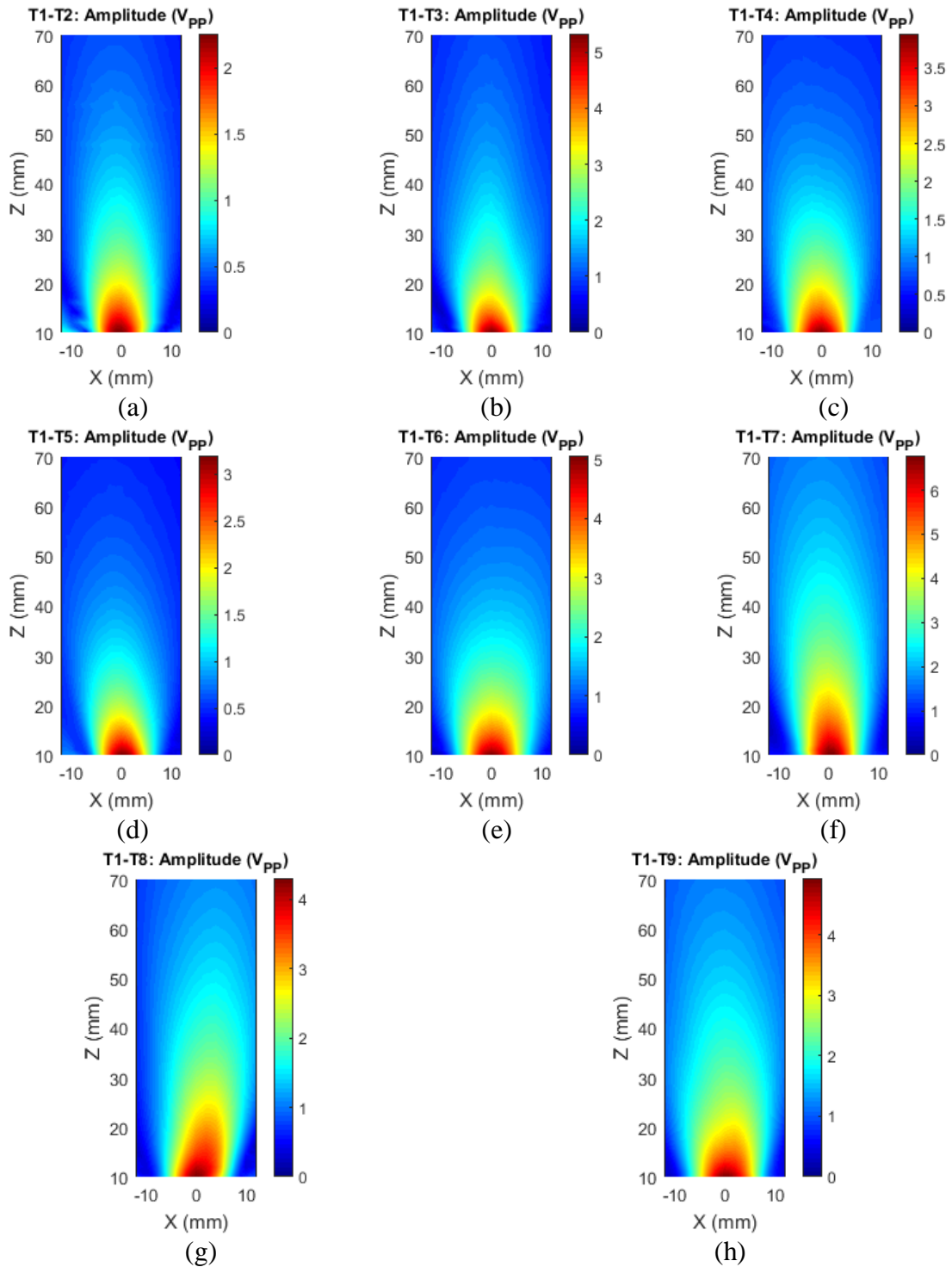
Transducer	S (V/MPa)
T2	21.2
T3	53.3
T4	34.4
T5	30.6
T6	43.2
T7	59.0
T8	31.6
T9	46.7

Source: Author.

4.2.5.2 Square pulse

Figure 29 shows the measured voltage distributions for T2-T9 when driving T1 with a square pulse. The distributions are similar to the ones created by a sinusoidal pulse (Figure 26), which means that the manufactured transducers have a narrow bandwidth response because the distribution shapes have a wide beam when it is compared to signals captured by the hydrophone (Figure 22).

Figure 29: Measured voltage distributions using transducers as receivers and driving T1 with a square pulse.

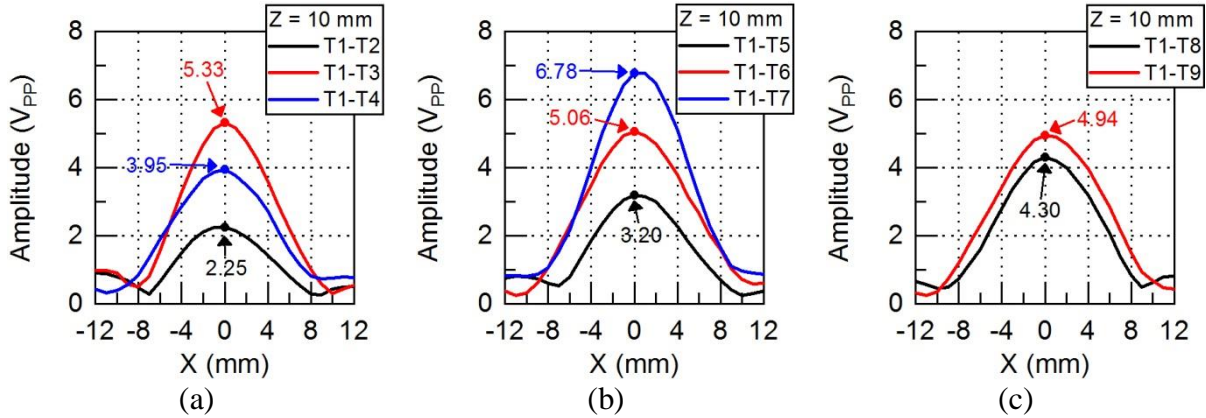


Source: Author.

Selecting $Z = 10$ mm, the measured voltage profiles in Figure 30 are also similar to measured voltage profiles from T2-T9 when T1 is driven by a sinusoidal pulse shown in Figure 27. The highest amplitude was captured by T7 (6.78 V_{PP}) and the smallest by T2 (2.25 V_{PP}), which results in a difference of 66.8 %. In addition, it can also be seen that there is

an amplitude recovery for $|X| > 6$ mm in all voltage profiles. Therefore, it is highly likely that this effect is caused by the PZT ceramic geometry, since it is more evidently when it is used transducers to transmit and receive ultrasound.

Figure 30: Measured voltage profiles at $Z = 10$ mm when receiving with transducers and driving T1 with a square pulse.



Source: Author.

Using the measured acoustic pressure generated by T1 when it was driven by a square pulse, the sensitivity (Table 5) of T2-T9 was also calculated so that it could be compared to the sensitivity values in Table 4. The sensitivity of all transducers decreased, proving that the manufactured transducers are not appropriate for capturing high frequencies. Otherwise, calculated sensitivities from both sinusoidal and square pulse would have presented the same for all transducers.

Table 5: Calculated when driving the transducers with a square pulse.

Transducer	S (V/MPa)
T2	15.24
T3	36.0
T4	26.7
T5	21.6
T6	34.1
T7	45.8
T8	29.0
T9	33.4

Source: Author.

For both pulse-echo and transmitting-receiving measurements, it was proven that the matching layer mixture was not well-homogenized and it did not present the same acoustic properties for all transducers. Moreover, Webster (2009) shows that manufacturing

transducers by handmade process are not very accurate, and that the matching and backing layers have their own manufacturing methods, improving the homogenization.

Despite having inaccuracies in the manufacturing process and all transducers presenting resonance frequency lower than the expected 500 kHz, it is still an advantage because for lung monitoring applications, lower frequency is preferred (RUETER et al., 2010). Therefore, radial modes can be taken as an advantage for low frequency transducers and the design of equipment to properly mix epoxy with high proportion of alumina can improve the transmitting and receiving responses of all transducers.

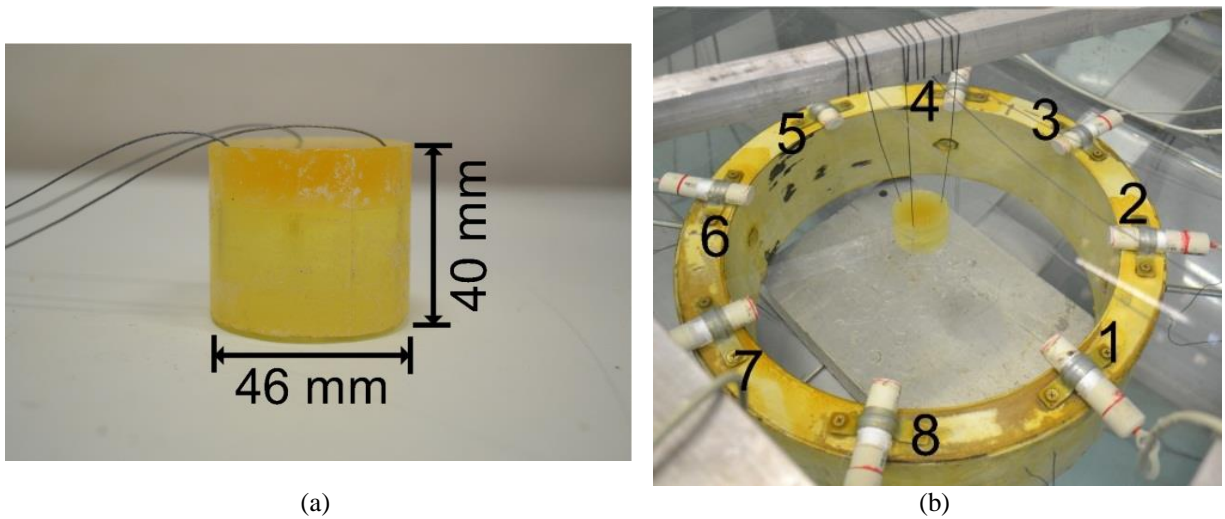
4.3 Manufactured test bench

Figure 31 (a) shows the manufactured phantom and its dimensions. First, the total mixture to make the phantom was poured into the PVC tube. However, because of an exothermic reaction of epoxy and its hardener, the temperature reached high levels that the mixture started bubbling. Then, to avoid high temperatures, another phantom was made with the total mixture divided into four parts.

The phantom does not present the desired thickness of 5 cm due to a leaking during the manufacturing process. Figure 31 (b) shows the test bench inside a tank with the 8 mono-element transducers and the manufactured phantom. In this case, the phantom is placed at the position B.

For a first version of the UST system, the wooden cylinder was a low-cost option to assemble the test bench so that the first signals based on UST could be recorded. However, despite using components to waterproof the wooden cylinder, the test bench may not be suitable for further experiments. Therefore, a new test bench based on a PVC cylinder has been designed in order to replace the wooden cylinder.

Figure 31: (a) Manufactured phantom and (b) the test bench after assembling.



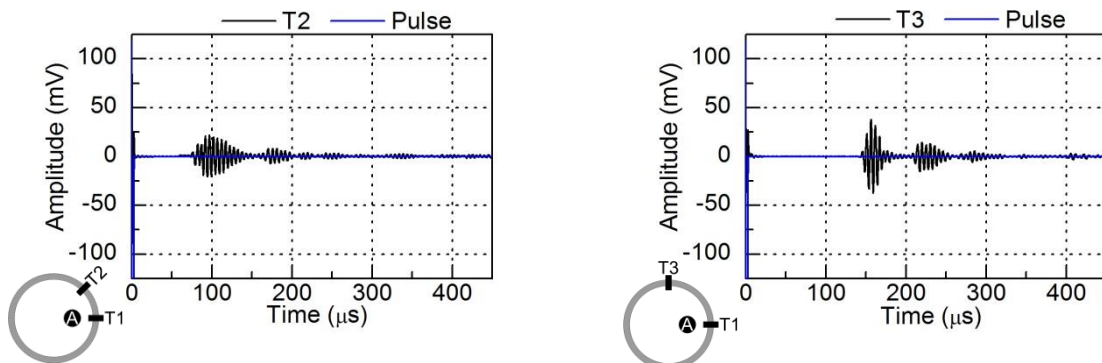
Source: Author.

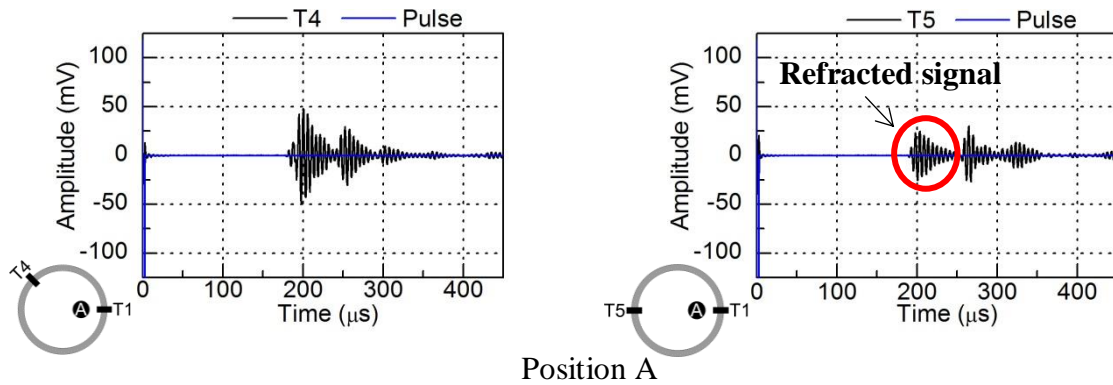
4.4 Evaluation of the test bench

Figure 32-35 illustrate the captured signals of T2, T3, T4 and T5, and the pulse generated by the pulser to drive T1 when the phantom is placed at positions A, B, C and D. In addition, signals were captured with no phantom placed inside the test bench. There is a schematic showing the position of the emitter, receiver and phantom on the bottom left of each figure.

The amplitude captured by T5, when the phantom is placed at position A (Figure 32), is smaller than its amplitude with no phantom (Figure 36), indicating that the signal passed throughout the phantom. Moreover, the signals T2 and T4 suffered no influence of the phantom presence when it was at positions A and C.

Figure 32: Recorded signals with phantom at position A.





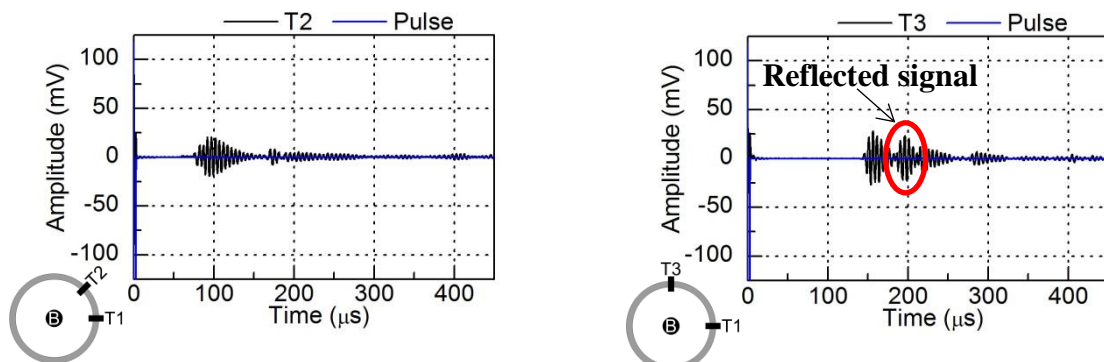
Source: Author.

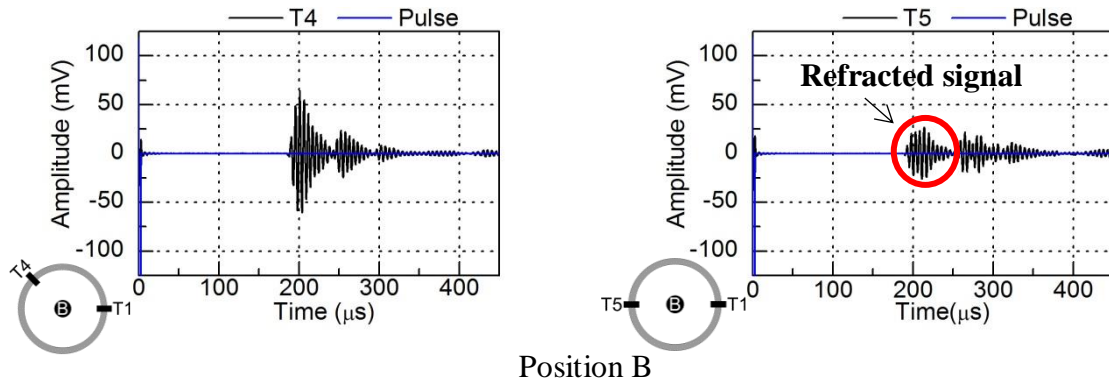
When the phantom was placed at position D, the captured signal by T4 suffered influence of the phantom, resulting on its attenuation whereas the signals captured by T2, T3, and T5 have almost the same amplitude when it is compared to the no phantom signals. Therefore, comparing the signals which were captured with the phantom at positions A, B, C, and D, the displacement of the phantom could be detected.

Figure 33 shows the captured signals for the phantom at position B. Most captured signals do not suffer any change compared to those presented in Figure 32, except for the captured signal by T3. It can be seen the presence of a reflected signal from the phantom, showing that both refracted and reflected signals can be captured, which are important for transmission and reflection reconstruction imaging algorithms (KAK; SLANEY, 2001).

When the phantom was placed at position D, the captured signal by T4 suffered influence of the phantom, resulting on its attenuation whereas the signals captured by T2, T3, and T5 have almost the same amplitude when it is compared to the no phantom signals. Therefore, comparing the signals which were captured with the phantom at positions A, B, C, and D, the displacement of the phantom could be detected.

Figure 33: Recorded signals with phantom at position B.

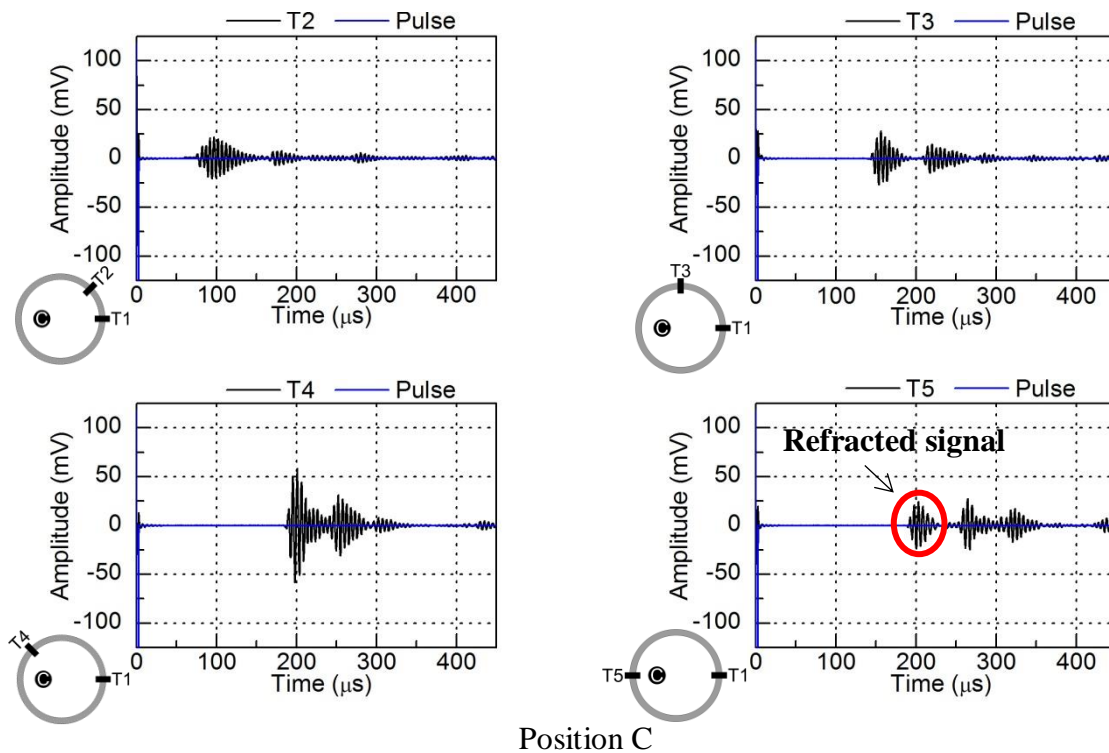




Source: Author.

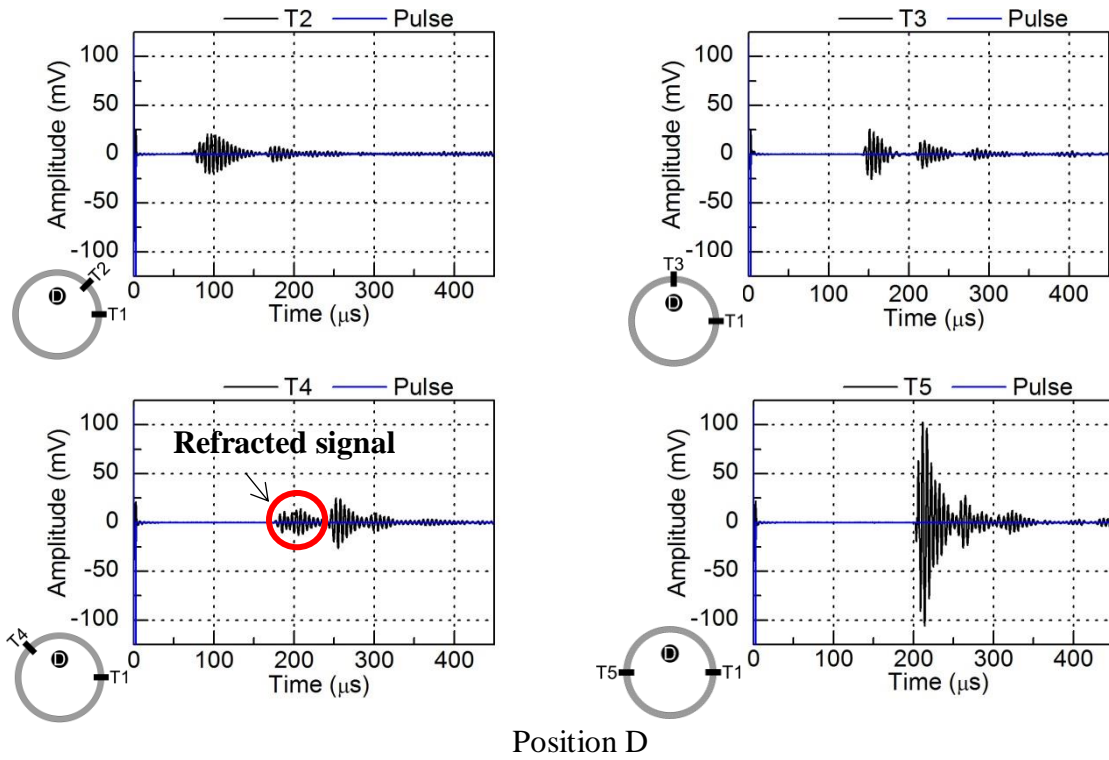
Analyzing only the signals with no phantom (Figure 36) inside the test bench, multiple peaks (2 and 3) can be seen. It happens because of signal reflections on the surface of the wooden cylinder and water, due to the spread of the transducer beam. These multiple peaks are present in the recorded signals with phantom at the positions A, B, C and D as well.

Figure 34: Recorded signals with phantom at position C



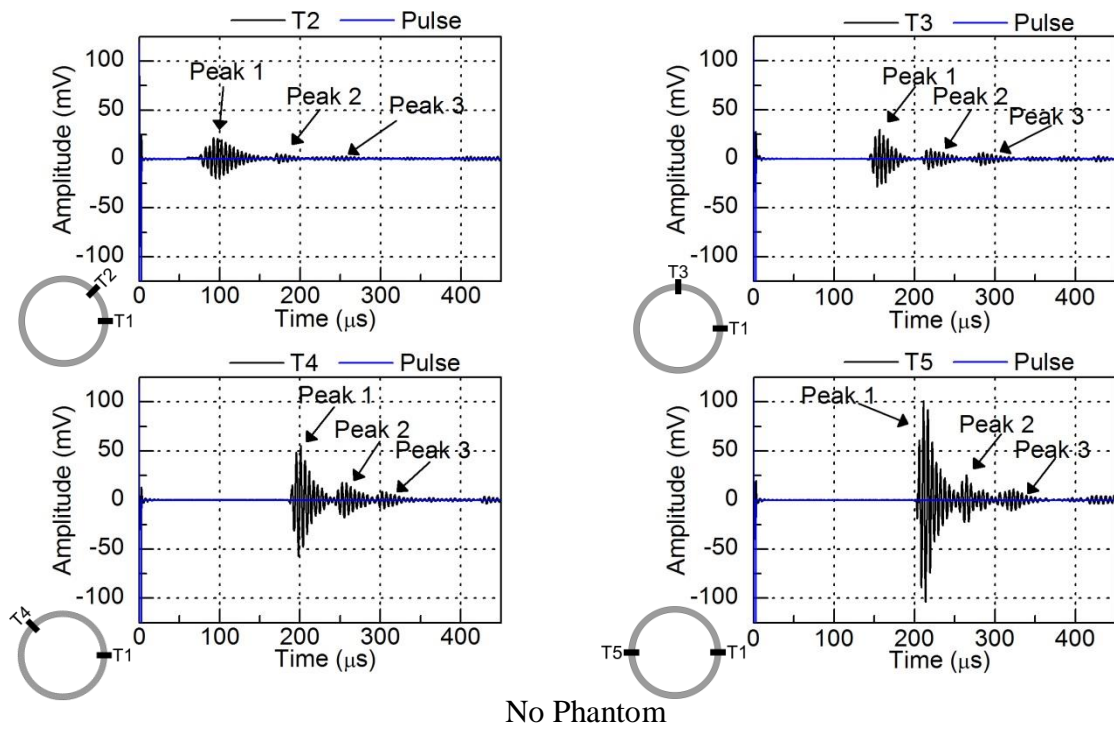
Source: Author.

Figure 35: Recorded signals with phantom at position D.



Source: Author.

Figure 36: Recorded signals with no phantom placed inside the test bench.

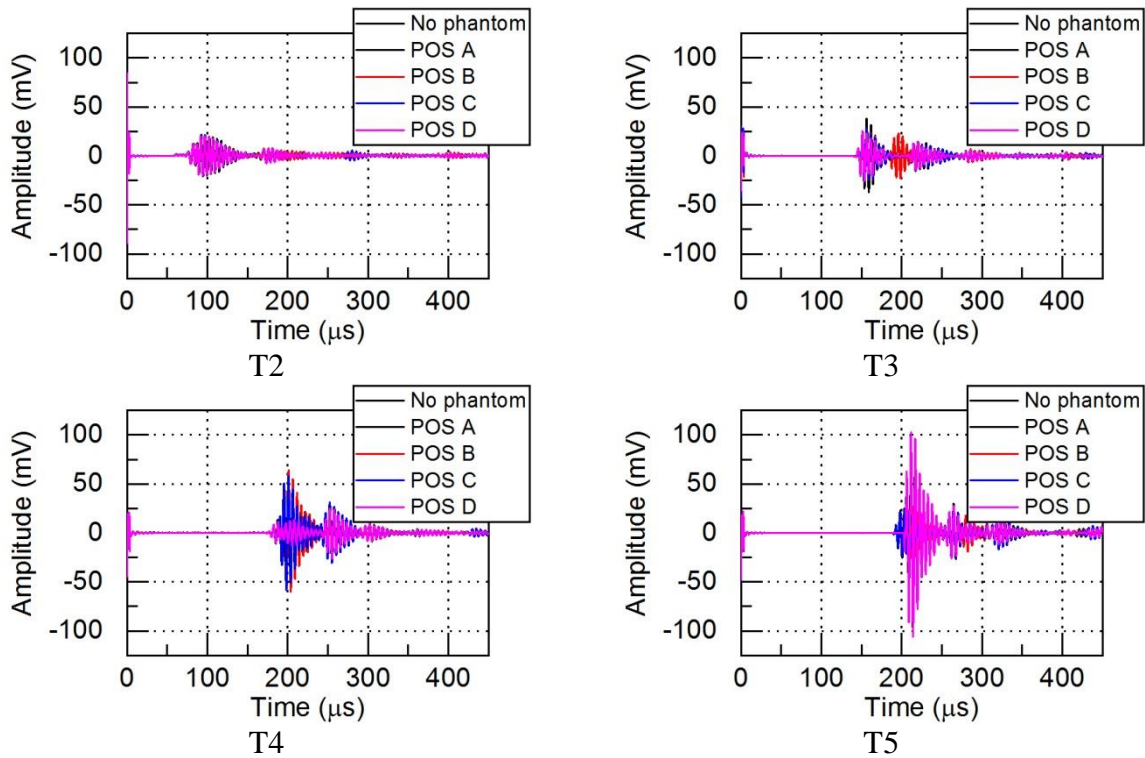


Source: Author.

Therefore, considering that the wooden cylinder wall is reflecting ultrasound, the same will happen with the thoracic wall. Thus, this first version of a test bench for an UST system can be used to develop reconstruction imaging algorithms.

Figure 37 shows the recorded signals individually for each transducer for comparison purpose. It can be seen that for the Peak 2 and 3, presented in Figure 36, there are no changes in their positions. Thus, it proves that these are signals that are reflected from the wooden cylinder wall, water surface, and the aluminum base from the test bench.

Figure 37: Recorded signals for each transducer.



Source: Author.

5 CONCLUSIONS

An experimental test bench for UST is still in development, but the first results already give information that this system can be used to develop imaging reconstruction algorithms. Moreover, signals can be captured with a distance of 300 mm from two face-to-face transducers.

When a phantom was placed inside the test bench, different signals for the four (A to D) positions of the phantom were captured, showing that the movement and position of an object can be determined inside of the test bench.

For the pulse-echo technique, the manufactured transducers presented resonance frequencies below 200 kHz with amplitudes smaller than 300 mV_{PP}. Meanwhile, the results from the transmitting-receiving technique showed that the manufactured transducers have a central frequency of 170 kHz.

Using the transmitting-receiving technique and driving all transducers with a 20 V_{PP} sinusoidal showed that each transducer operates differently regarding its amplitude response. The highest measured acoustic pressure was 28 kPa while the lowest stood at 9 kPa. Moreover, when driving all transducers with a 100 V_{PP} square pulse, it was measured a maximum acoustic pressure of 148 kPa. However, all the measured signals had harmonic content.

The effects seen in the amplitude responses were also observed in the sensitivity of each transducer, showing a linear relationship. The transducer which transmitted the highest acoustic pressure was also the one with the highest sensitivity and vice-verse. Thus, it proves that the matching layer influences equally the transmitting and receiving responses of all manufactured transducers.

The difference in amplitude responses are mainly given by the matching layer, which depends on its thickness and mixture proportion. Due to a high proportion of alumina, the mixture homogenization with epoxy resin could not be done properly by a handmade process. Thus, the manufacturing processes of the matching layer have to be improved to reduce the difference between the transducer responses, which leads to a better acoustic pressure transmission and sensitivity.

The manufactured transducers have a length of 78 mm, making these transducers not viable for clinical applications. Nevertheless, all transducers can still be used for prototype

systems of UST to transmit and capture signals in order to improve the test bench and to provide data for reconstruction imaging algorithms.

6 REFERENCES

- AMATO, Marcelo B. P. et al. Driving Pressure and Survival in the Acute Respiratory Distress Syndrome. **New England Journal of Medicine**, [S. l.], v. 372, n. 8, p. 747–755, 2015. DOI: 10.1056/NEJMsa1410639.
- ASHBAUGH, D. G.; BIGELOW, D. B.; PETTY, T. L.; LEVINE, B. E. Acute respiratory distress in adults. **Lancet**, [S. l.], v. 2, n. 7511, p. 319–323, 1967. DOI: 10.1016/s0140-6736(67)90168-7.
- BALL, Lorenzo; VERCESI, Veronica; COSTANTINO, Federico; CHANDRAPATHAM, Karthikka; PELOSI, Paolo. Lung imaging: How to get better look inside the lung. **Annals of Translational Medicine**, [S. l.], v. 5, n. 14, 2017. DOI: 10.21037/atm.2017.07.20.
- BERTONI, Michele; SPADARO, Savino; GOLIGHER, Ewan C. Monitoring Patient Respiratory Effort during Mechanical Ventilation: Lung and Diaphragm-Protective Ventilation. **Critical Care**, [S. l.], v. 24, n. 1, p. 106, 2020. DOI: 10.1186/s13054-020-2777-y.
- CASCELLA, Marco; RAJNIK, Michael; CUOMO, Arturo; DULEBOHN, Scott C.; DI NAPOLI, Raffaella. **Features, Evaluation and Treatment Coronavirus (COVID-19) [Updated 2020 Apr 6]**. [s.l.] : StatPearls Publishing, 2020.
- CHENG, Vincent C. C.; LAU, Susanna K. P.; WOO, Patrick C. Y.; KWOK, Yung Yuen. **Severe Acute Respiratory Syndrome Coronavirus as an Agent of Emerging and Reemerging Infection****Clinical Microbiology Reviews**. American Society for Microbiology (ASM), , 2007. DOI: 10.1128/CMR.00023-07.
- CINEL, I.; JEAN, S.; DELLINGER, R. P. Dynamic lung imaging techniques in mechanically ventilated patients. *In: Intensive Care Medicine: Annual Update 2007*. [s.l.] : Springer New York, 2007. p. 371–380. DOI: 10.1007/978-0-387-49518-7_33.
- DURIC, Neb et al. Breast imaging with the SoftVue imaging system: first results. *In: Medical imaging 2013: ultrasonic imaging, tomography, and therapy 2013*, SPIE, 2013. p. 86750K. DOI: 10.1117/12.2002513.
- FAN, Eddy et al. An Official American Thoracic Society/European Society of Intensive Care Medicine/Society of Critical Care Medicine Clinical Practice Guideline: Mechanical Ventilation in Adult Patients with Acute Respiratory Distress Syndrome. **ATS Journals**, [S. l.], 2017. DOI: 10.1164/rccm.201703-0548ST.
- GEMMEKE, Hartmut; HOPP, Torsten; ZAPF, Michael; KAISER, Clemens; RUITER, Nicole V. 3D ultrasound computer tomography: Hardware setup, reconstruction methods and first

clinical results. **Nuclear Instruments and Methods in Physics Research, Section A: Accelerators, Spectrometers, Detectors and Associated Equipment**, [S. l.], v. 873, p. 59–65, 2017. DOI: 10.1016/j.nima.2017.07.019.

KAK, Avinash C.; SLANEY, Malcolm. **Principles of Computerized Tomographic Imaging**. [s.l.] : Society for Industrial and Applied Mathematics, 2001. DOI: 10.1137/1.9780898719277.

KINSLER, Lawrence E.; FREY, Austin R.; COPPENS, Alen B.; SANDERS, James V. **Fundamentals of Acoustics**. 4. ed. [s.l.] : John Wiley & Sons, 2000. DOI: 10.1016/j.agee.2008.10.017.

KUNKEL, H. A.; LOCKE, S.; PIKEROEN, B. Finite-Element Analysis of Vibrational Modes in Piezoelectric Ceramic Disks. **IEEE Transactions on Ultrasonics, Ferroelectrics, and Frequency Control**, [S. l.], v. 37, n. 4, p. 316–328, 1990. DOI: 10.1109/58.56492.

LAI, Chih Cheng; SHIH, Tzu Ping; KO, Wen Chien; TANG, Hung Jen; HSUEH, Po Ren. Severe acute respiratory syndrome coronavirus 2 (SARS-CoV-2) and coronavirus disease-2019 (COVID-19): The epidemic and the challenges *International Journal of Antimicrobial Agents*. **Elsevier**, 2020. DOI: 10.1016/j.ijantimicag.2020.105924.

LIAN, Jin Xiong. Using ventilator waveforms to optimize patient-ventilator interaction. **Nursing Critical Care**, [S. l.], v. 5, n. 5, p. 14–24, 2010. DOI: 10.1097/01.ccn.0000387132.04492.2d.

LIPSON, David A.; BEEK, Edwin J. R. van. **Functional lung imaging**. 1. ed. [s.l.] : CRC Press, 2005.

NIEMAN, Gary F.; SATALIN, Joshua; ANDREWS, Penny; AIASH, Hani; HABASHI, Nader M.; GATTO, Louis A. Personalizing mechanical ventilation according to physiologic parameters to stabilize alveoli and minimize ventilator induced lung injury (VILI). **Intensive Care Medicine Experimental**, [S. l.], v. 5, n. 1, 2017. DOI: 10.1186/s40635-017-0121-x.

RAGALLER, Maximillian; RICHTER, Torsten. Acute lung injury and acute respiratory distress syndrome. *In: Journal of emergencies, trauma and shock 2010*, Wolters Kluwer -- Medknow Publications, 2010. p. 43–51. DOI: 10.4103/0974-2700.58663.

RIERA, J.; RIU, P. J.; CASAN, P.; MASCLANS, J. R. Electrical impedance tomography in acute lung injury. **Medicina Intensiva (English Edition)**, [S. l.], v. 35, n. 8, p. 509–517, 2011. DOI: 10.1016/j.medine.2011.11.004.

ROY, O.; ZUBERI, M. A. H.; PRATT, R. G.; DURIC, N. Ultrasound breast imaging using frequency domain reverse time migration. *In: Medical imaging 2016: ultrasonic imaging*

and tomography 2016, SPIE, 2016. p. 97900B. DOI: 10.1117/12.2218366.

RUETER, D.; HAUBER, H. P.; DROEMAN, D.; ZABEL, P.; UHLIG, Stefan. Low-frequency ultrasound permeates the human thorax and lung: A novel approach to non-invasive monitoring. **Ultraschall in der Medizin**, [S. l.], v. 31, n. 1, p. 53–62, 2010. DOI: 10.1055/s-0028-1109482.

RYMARCZYK, Tomasz; GOŁĄBEK, Michał; BOŹEK, Piotr; ADAMKIEWICZ, Przemysław; MAJ, Michał; SIKORA, Jan. Ultrasound tomography measuring system for acquisition and analysis data. **Przegląd Elektrotechniczny**, [S. l.], v. 95, n. 3, p. 111–114, 2019. DOI: 10.15199/48.2019.03.26.

SONG, Junjie; WANG, Shanshan; ZHOU, Liang; PENG, Yang; DING, Yang; YUCHI, Ming. A Prototype System for Ultrasound Computer Tomography with Ring Array. In: **2nd IET international conference on biomedical image and signal processing (icbisp 2017) 2017**, Institution of Engineering and Technology, 2017. p. 9 (4 .)-9 (4 .). DOI: 10.1049/cp.2017.0085.

SONG, Xiaoqian; LI, Maokun; YANG, Fan; XU, Shenheng; ABUBAKAR, Aria. Feasibility study of acoustic imaging for human thorax using an acoustic contrast source inversion algorithm. **The Journal of the Acoustical Society of America**, [S. l.], v. 144, n. 5, p. 2782–2792, 2018. DOI: 10.1121/1.5078590.

STOTZKA, Rainer; WUERFEL, Jan; MUELLER, Tim O.; GEMMEKE, Hartmut. Medical imaging by ultrasound computer tomography. In: **Medical imaging 2002: ultrasonic imaging and signal processing 2002**, SPIE, 2002. p. 110–119. DOI: 10.1117/12.462144.

TOMICIC, Vinko; CORNEJO, Rodrigo. Lung monitoring with electrical impedance tomography: Technical considerations and clinical applications. **Journal of Thoracic Disease**, [S. l.], v. 11, n. 7, p. 3122–3135, 2019. DOI: 10.21037/jtd.2019.06.27.

WAAG, Robert C.; FEDEWA, Russell J. A ring transducer system for medical ultrasound research. **IEEE Transactions on Ultrasonics, Ferroelectrics, and Frequency Control**, [S. l.], v. 53, n. 10, p. 1707–1718, 2006. DOI: 10.1109/TUFFC.2006.104.

WANG, Li-sheng; WANG, Yi-ru; YE, Da-wei; LIU, Qing-quan. Review of the 2019 Novel Coronavirus (COVID-19) based on current evidence. **International Journal of Antimicrobial Agents**, [S. l.], p. 105948, 2020. DOI: 10.1016/j.ijantimicag.2020.105948.

WEBSTER, Rhiannon Alys. Passive materials for high frequency piezocomposite ultrasonic transducers. **University of Birmingham, Birmingham**, 2009.

YANG, Xiaobo et al. Clinical course and outcomes of critically ill patients with SARS-CoV-2

pneumonia in Wuhan, China: a single-centered, retrospective, observational study. **The Lancet**, 2020. DOI: 10.1016/S2213-2600(20)30079-5.